

**Leveraging Ligand Steric Demand to Control Linker Exchange and Fine-Tune Domain  
Building Block Composition in Stratified Metal-Organic Frameworks**

by

**Mattheus De Souza**

BSc, The College of New Jersey, 2018

Submitted to the Graduate Faculty of the  
Dietrich School of Arts and Sciences in partial fulfillment  
of the requirements for the degree of  
Master of Science

University of Pittsburgh

2021

UNIVERSITY OF PITTSBURGH

DIETRICH SCHOOL OF ARTS AND SCIENCES

This thesis was presented

by

**Matheus De Souza**

It was defended on

April 29, 2021

and approved by

Dr. Jill Millstone, Associate Professor, Department of Chemistry

Dr. Raúl Hernández Sánchez, Assistant Professor, Department of Chemistry

Dr. Nathaniel Rosi, Professor, Department of Chemistry

Thesis Advisor Director: Dr. Nathaniel Rosi, Professor, Department of Chemistry

Copyright © by Matheus De Souza

2021

# **Leveraging Ligand Steric Demand to Control Linker Exchange and Fine-Tune Domain Building Block Composition in Stratified Metal-Organic Frameworks**

Matheus De Souza, MS

University of Pittsburgh, 2021

Incorporation of a variety of components into structural and functional domains within metal-organic frameworks (MOFs) has been shown to reveal new properties that expand the scope of potential applications. Stratified MOFs (sMOFs) are a class of multicomponent MOFs consisting of two or more compositionally unique concentric domains (strata). sMOFs can be encoded with unparalleled complexity through the partitioning of structural components into domain building blocks (DBBs). However, the labile nature of metal-linker coordination in MOFs handicaps achieving pristine DBBs with varied linkers due to linker exchange reactions that occur simultaneously with secondary strata growth. Therefore, to achieve more complex sMOF compositions, it is vital to characterize and control the competing processes of both strata growth and linker exchange. This work presents a systematic study of how linker exchange can be controlled and mitigated in UiO-67 sMOFs by tuning the steric demand of linkers and length of secondary growth reactions. Post-synthetic soaking experiments revealed solvents in which sMOFs maintain compositional integrity for up to 13 months and more stringent environments that result in a homogenous mixture of linkers within 2 hours. We also report a new approach to sMOF synthesis that allows for mitigation of linker exchange between two non-sterically hindered linkers. We present and employ a quantitative method for assessing and visualizing the outcomes

of the competing processes of strata growth and ligand exchange that relies on elemental mapping via scanning transmission electron microscopy energy-dispersive X-ray spectroscopy.

## Table of Contents

<b>1.0 Introduction</b> .....	1
<b>1.1 Design, Structure, and Function</b> .....	1
<b>1.2 Supramolecular Coordination Chemistry</b> .....	2
<b>1.3 Metal-Organic Frameworks</b> .....	4
<b>1.4 Stratified Metal-Organic Frameworks</b> .....	5
<b>2.0 Control of Linker Exchange to Fine-Tune Stratified Metal Organic Framework</b>	
<b>Composition</b> .....	7
<b>2.1 Introduction</b> .....	7
<b>2.2 Results and Discussion</b> .....	8
<b>2.3 Conclusion</b> .....	17
<b>3.0 Experimental Section</b> .....	18
<b>3.1 General Methods</b> .....	18
<b>3.2 Synthesis and Characterization of Organic Linkers</b> .....	19
<b>3.2.1 Dimethyl 2-nitro-1,1'-biphenyl-4,4'-dicarboxylate (1)</b> .....	19
<b>3.2.2 Dimethyl 2-amino-1,1'-biphenyl-4,4'-dicarboxylate (2)</b> .....	19
<b>3.2.3 2-acetamido-1,1'-biphenyl-4,4'-dicarboxylate (3)</b> .....	20
<b>3.2.4 2-(tert-butoxycarbonylamino)-1,1'-biphenyl-4,4'-dicarboxylate (4)</b> .....	23
<b>3.2.5 (S)-2-(1-(tert-butoxycarbonyl)pyrrolidine-2-carboxamido)-1,1'-biphenyl-4,4'-dicarboxylic acid (5)</b> .....	23
<b>3.2.6 2,2'-Bipyridine-5,5'-dicarboxylic acid (6)</b> .....	23
<b>3.3 Synthesis and Characterization of Metal Organic Frameworks</b> .....	24

3.3.1 Synthesis of Bpy-UiO-67(Zr) seed crystallites .....	24
3.3.2 Calibration of EDS for palladium detection .....	26
3.3.3 Synthesis of Bpy-UiO-67(Zr) $\subset$ UiO-67(Zr) sMOF .....	27
3.3.4 Synthesis of Bpy-UiO-67(Zr) $\subset$ N-Acetyl-UiO-67(Zr) sMOF .....	32
3.3.5 Synthesis of Bpy-UiO-67(Zr) $\subset$ N-boc-UiO-67(Zr) sMOF .....	36
3.3.6 Synthesis of Bpy-UiO-67(Zr) $\subset$ Proline-boc-UiO-67(Zr) sMOF .....	42
3.3.7 Synthesis of Bpy-UiO-67(Zr) $\subset$ Proline-boc-UiO-67(Zr) $\subset$ UiO-67(Zr) sMOF .....	48
3.4 Strata Stability in Solvent .....	49
3.4.1 Stability of Bpy-UiO-67(Zr) $\subset$ UiO-67(Zr) in DMF at 100 °C .....	50
3.4.2 Stability of Bpy-UiO-67(Zr) $\subset$ UiO-67(Zr) in water at 85 °C .....	52
3.4.3 Stability of Bpy-UiO-67(Zr) $\subset$ UiO-67(Zr) in DMF and CH <sub>3</sub> COOH at 65 °C .....	54
Appendix A Reproduction Permissions .....	55
Bibliography .....	56

## List of Tables

<b>Table 3.1 Shell palladium to zirconium ratio calculated using STEM-EDS for Bpy(Pd)-UiO-67(Zr) <math>\subset</math> UiO-67(Zr) synthesized with different reaction times.....</b>	<b>29</b>
<b>Table 3.2 Shell palladium to zirconium ratio calculated using STEM-EDS for Bpy(Pd)-UiO-67(Zr) <math>\subset</math> N-Acetyl-UiO-67(Zr) synthesized with different reaction times. ....</b>	<b>34</b>
<b>Table 3.3 Shell palladium to zirconium ratio calculated using STEM-EDS for Bpy(Pd)-UiO-67(Zr) <math>\subset</math> N-boc-UiO-67(Zr) synthesized with different reaction lengths.....</b>	<b>39</b>
<b>Table 3.4 Shell palladium to zirconium ratio calculated using STEM-EDS for Bpy(Pd)-UiO-67(Zr) <math>\subset</math> Proline-boc-UiO-67(Zr) synthesized with different reaction lengths. Shells observed after 10 minutes of reaction were not thick enough to get accurate reading. .....</b>	<b>45</b>

## List of Figures

Figure 1.1 (A) Scheme of a square complex self-assembly and (B) illustrations of 3D metal-organic polyhedra Adapted with permission. <sup>20</sup> Copyright 2005, American Chemical Society. ....	3
Figure 1.2 Examples of isorecticular series of MOFs based on MOF-5 depicting tuning of pore environment whilst maintaining cubic framework. Adapted with permission. <sup>28</sup> Copyright 2002, AAAS. ....	5
Figure 2.1 Illustrations of possible linker arrangements resulting from secondary growth reaction with 2-D depictions of linker distributions below each example. ....	8
Figure 2.2 Stepwise procedure from seed Bpy-UiO-67(Zr) to post-metalation core-shell Bpy(Pd)-UiO-67(Zr)⊂R1-UiO-67(Zr) with chemical structures of R1 functional groups illustrated. ....	9
Figure 2.3 HAADF images of Bpy(Pd)-UiO-67(Zr)⊂(I-IV)-UiO-67(Zr) with reaction times between 10 minutes and 5 hours. *Bpy(Pd)-UiO-67(Zr)⊂(I)-UiO-67(Zr) after 4 hours of reaction. ....	11
Figure 2.4 Shell Pd to Zr ratio with respect to reaction time in minutes for Bpy(Pd)-UiO-67(Zr)⊂R1-UiO-67(Zr).....	13
Figure 2.5 (A) HAADF image and (B) EDS line-scan (Zr, red; Pd, green) of Bpy(Pd)-UiO-67(Zr)⊂(I)-UiO-67(Zr) after 20 minutes of shell growth. (C) HAADF image of Bpy(Pd)-UiO-67(Zr)⊂(IV)-UiO-67(Zr) after 5 minutes of shell growth. (D) HAADF image and (E) EDS line-scan of Bpy(Pd)-UiO-67(Zr)⊂(IV)-UiO-67(Zr)⊂(I)-UiO-67(Zr) after 20 minutes of shell growth. ....	14

**Figure 2.6 (A) HAADF images of Bpy(Pd)-UiO-67(Zr)⊂(I)-UiO-67(Zr) before and after soaking in DMF, ACN and hexanes for up to 13 months and a plot of the shell Pd to Zr ratio over time and (B) HAADF images and EDS line-scans (Zr, red; Pd, green) of Bpy(Pd)-UiO-67(Zr)⊂(I)-UiO-67(Zr) before and after soaking in DMF and acetic acid at 65 °C for two hours. .... 16**

**Figure 3.1 Simulated PXRD pattern of UiO-67(Zr) (black) and experimental PXRD of as synthesized Bpy-UiO-67(Zr) seed crystallites (red). .... 25**

**Figure 3.2 TEM image (A) and size distribution (B) of Bpy-UiO-67(Zr) seed crystallites having an average diameter of 341±31 nm (n=100 counts). .... 25**

**Figure 3.3 Palladium to zirconium ratios of mixed linker Bpy-R%-UiO-67(Zr) MOFs with trendlines made for R% 0 – 50% (black) and R% 60 – 100% (red). .... 27**

**Figure 3.4 Simulated PXRD pattern of UiO-67(Zr) (black) and experimental PXRD of as synthesized Bpy-UiO-67(Zr) ⊂ UiO-67(Zr) sMOF (red). .... 28**

**Figure 3.5 HAADF TEM images of Bpy(Pd)-UiO-67(Zr) ⊂ UiO-67(Zr) sMOFs after (A) 10 minutes, (B) 20 minutes, (C) 60 minutes, and (D) 4 hours of reaction time. .... 30**

**Figure 3.6 STEM-EDS line-scans of Bpy(Pd)-UiO-67(Zr) ⊂ UiO-67(Zr) sMOFs (Zr, red; Pd, green) after (A) 10 minutes, (B) 20 minutes, (C) 60 minutes, and (D) 4 hours of reaction time. .... 31**

**Figure 3.7 Simulated PXRD pattern of UiO-67(Zr) (black) and experimental PXRD of as synthesized Bpy-UiO-67(Zr) ⊂ N-Acetyl-UiO-67(Zr) sMOF(red). .... 33**

**Figure 3.8 TEM images of (A) Bpy-UiO-67(Zr) seed crystallites and Bpy-UiO-67(Zr) ⊂ N-Acetyl-UiO-67(Zr) sMOFs after (B) 10 minutes, (C) 20 minutes, (D) 60 minutes, (E) 2 hours, and (F) 5 hours of reaction time. .... 34**

**Figure 3.9 HAADF TEM images of Bpy(Pd)-UiO-67(Zr)  $\subset$  N-Acetyl-UiO-67(Zr) sMOFs after (A) 10 minutes, (B) 20 minutes, (C) 60 minutes, (D) 2 hours, and (E) 5 hours of reaction time..... 35**

**Figure 3.10 STEM-EDS line-scans of Bpy(Pd)-UiO-67(Zr)  $\subset$  N-Acetyl-UiO-67(Zr) sMOFs (Zr, red; Pd, green) after (A) 10 minutes, (B) 20 minutes, (C) 60 minutes, (D) 2 hours, and (E) 5 hours of reaction time..... 36**

**Figure 3.11 Simulated PXRD pattern of UiO-67(Zr) (black) and experimental PXRD of as synthesized Bpy-UiO-67(Zr)  $\subset$  N-boc-UiO-67(Zr) sMOF (red)..... 37**

**Figure 3.12 TEM images of (A) Bpy-UiO-67(Zr) seed crystallites and Bpy-UiO-67(Zr)  $\subset$  N-boc-UiO-67(Zr) sMOFs after (B) 10 minutes, (C) 20 minutes, (D) 60 minutes, (E) 2 hours, (F) 5 hours, (G) 24 hours, (H) and 48 hours of reaction time. .... 38**

**Figure 3.13 HAADF TEM images of Bpy(Pd)-UiO-67(Zr)  $\subset$  N-boc-UiO-67(Zr) sMOFs after (A) 10 minutes, (B) 20 minutes, (C) 60 minutes, (D) 2 hours, (E) 5 hours, (F) 24 hours, and (G) 48 hours of reaction time..... 40**

**Figure 3.14 STEM-EDS line-scans of Bpy(Pd)-UiO-67(Zr)  $\subset$  N-boc-UiO-67(Zr) sMOFs (Zr, red; Pd, green) after (A) 10 minutes, (B) 20 minutes, (C) 60 minutes, (D) 2 hours, (E) 5 hours, (F) 24 hours, and (G) 48 hours of reaction time..... 41**

**Figure 3.15 Simulated PXRD pattern of UiO-67(Zr) (black) and experimental PXRD of as synthesized Bpy-UiO-67(Zr)  $\subset$  Proline-boc-UiO-67(Zr) sMOF (red). .... 43**

**Figure 3.16 TEM images of (A) Bpy-UiO-67(Zr) seed crystallites and Bpy-UiO-67(Zr)  $\subset$  Proline-boc-UiO-67(Zr) sMOFs after (B) 10 minutes, (C) 20 minutes, (D) 60 minutes, (E) 2 hours, (F) 5 hours, (G) 24 hours, (H) and 48 hours of reaction time. .... 44**

**Figure 3.17 HAADF TEM images of Bpy(Pd)-UiO-67(Zr)  $\subset$  Proline-boc-UiO-67(Zr) sMOFs after (A) 10 minutes, (B) 20 minutes, (C) 60 minutes, (D) 2 hours, (E) 5 hours, (F) 24 hours, and (G) 48 hours of reaction time..... 46**

**Figure 3.18 STEM-EDS line-scans of Bpy(Pd)-UiO-67(Zr)  $\subset$  Proline-boc-UiO-67(Zr) sMOFs (Zr, red; Pd, green) after (A) 10 minutes, (B) 20 minutes, (C) 60 minutes, (D) 2 hours, (E) 5 hours, (F) 24 hours, and (G) 48 hours of reaction time..... 47**

**Figure 3.19 Shell palladium to zirconium ratios of Bpy(Pd)-UiO-67(Zr)  $\subset$  N-boc-UiO-67(Zr) (green) and Bpy(Pd)-UiO-67(Zr)  $\subset$  Proline-boc-UiO-67(Zr) (orange) sMOFs for reaction times of up to 48 hours long. .... 48**

**Figure 3.20 HAADF TEM images of Bpy(Pd)-UiO-67(Zr)  $\subset$  UiO-67(Zr) sMOFs (A) before soaking and (B) 48 hours of soaking in DMF at 100 °C. .... 50**

**Figure 3.21 Shell palladium to zirconium ratio of Bpy(Pd)-UiO-67(Zr)  $\subset$  UiO-67(Zr) sMOFs soaked in DMF at 100 °C for up to 48 hours..... 51**

**Figure 3.22 HAADF TEM images of Bpy(Pd)-UiO-67(Zr)  $\subset$  UiO-67(Zr) sMOFs (A) before soaking and (B) 21 hours of soaking in water at 85 °C. .... 52**

**Figure 3.23 Simulated PXRD pattern of UiO-67(Zr) (black) and experimental PXRD of Bpy-UiO-67(Zr)  $\subset$  UiO-67(Zr) sMOF after 21 hours of soaking in water at 85 °C (red).53**

**Figure 3.24 Simulated PXRD pattern of UiO-67(Zr) (black) and experimental PXRD of Bpy-UiO-67(Zr)  $\subset$  UiO-67(Zr) sMOF after 2 hours of soaking in DMF and CH<sub>3</sub>COOH at 65 °C (red)..... 54**

## **1.0 Introduction**

### **1.1 Design, Structure, and Function**

Chemistry, by definition, is the study of the composition, structure and properties of matter. An essential component to chemistry research is molecular synthesis: the process by which chemical reactions are designed and performed to alter the composition of reactants and achieve one or multiple new products. Synthesis can also be described as the application of chemistry, in that it applies the knowledge garnered on different elements and properties of matter to develop safe conditions for chemical reactions to reproducibly synthesize target molecules. Molecular synthesis has expanded the fundamental understanding of chemical processes, contributing immensely to advancements in adjacent fields such as pharmacy. Modern drug design is at the intersection of medical science and chemistry. Knowledge of biological processes allows for the identification of target molecules while molecular synthesis is then relied upon to synthesize drugs that are complementary in charge and structure to the target molecule.<sup>1</sup> One can imagine that without molecular synthesis, continued studies in medical science would result in the identification of target drug molecules with no reliable method of achieving the desired structure and composition. In this dissertation, I emphasize the importance of devising synthetic pathways to reproducibly synthesize products with a desired structure and composition.

When we turn to nature, most of the processes we observe are driven by supramolecular systems, not individual molecules. While molecular synthesis has uncovered necessary information for selectively altering the composition of individual molecules, the same techniques cannot be applied to dictate the assembly of molecular building blocks into more complex

structures. Self-assembly is a process driven primarily by intermolecular forces in which molecular building blocks spontaneously form ordered supramolecular complexes, such as cells.<sup>2-4</sup> The human body, comprised of over 37 trillion cells at any time, serves as the gold standard of what is ultimately achievable through self-assembly.<sup>5</sup> The area of supramolecular chemistry has emerged to study the non-covalent interactions crucial to the assembly, structure, and function of complex systems.<sup>6-8</sup> The goal of supramolecular chemistry is to expand the precise control over composition, structure and properties beyond the molecule and into extended 2D and 3D structures.<sup>9-11</sup> The first reported self-assembled structures can be traced back to the discoveries of crown ethers, spherands, and cryptands in the 1960's.<sup>12-16</sup> The isolation of these supramolecular complexes displayed a novel ability to encode properties into molecules that promote molecular recognition of other building blocks and guide self-assembly. This particular method of using organic backbones however, leaves very little room for functionalization, as changes in composition would alter the properties that drive self-assembly.<sup>10,17</sup> Conversely, the discovery of end capped metal complexes as building blocks for the self-assembly of metal-organic compounds brought forth a new field of chemistry titled supramolecular coordination chemistry.<sup>18</sup>

## 1.2 Supramolecular Coordination Chemistry

A desire to incorporate 90° angles into organic frameworks prompted Fujita et al. to design a square macrocycle using linear bipyridine organic ligands to bridge end capped palladium (II) with a square planar geometry (Figure 1.1 A).<sup>19</sup> The overall +8 charge of the metal centers made the macrocycle water-soluble while the bridging ligands created a unique hydrophobic cavity. As a result, the coordination assembly displayed exceptional molecular recognition of hydrophobic

organic guest molecules in aqueous solutions.<sup>19,20</sup> Soon after, more complex polytopic organic ligands and end-capped metal building blocks were used to synthesize 3D metal-organic polyhedral with more intricately designed microporous properties (Figure 1.1 B).<sup>20-24</sup> While still considered a form of synthesis, design of metal-organic coordination compounds required an approach similar to that used in molecular synthesis. Once a desired assembly is identified, focus is spent on analyzing the vertices to identify potential molecular geometries capable of achieving the necessary angles. Possible organic ligands are then designed with added consideration for the identity, quantity, and placement of the metal coordinating functional groups. This approach has presented a practical method of synthesizing coordination assemblies with judiciously designed pore-environments that promote specific host-guest interactions. These principles were further expanded by bridging symmetrical metal ions and clusters with organic ligands into extended microporous coordination assemblies called metal-organic frameworks.<sup>25,26</sup>

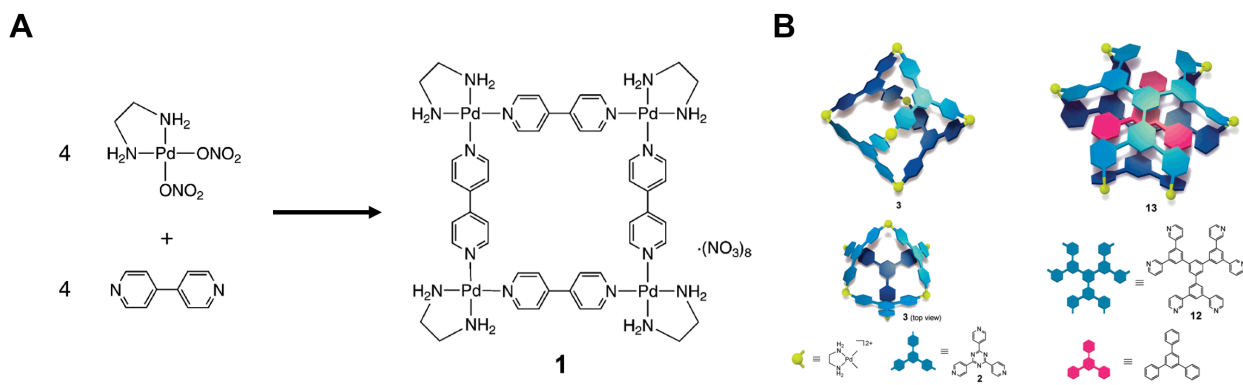


**Figure 1.1 (A) Scheme of a square complex self-assembly and (B) illustrations of 3D metal-organic polyhedra**

Adapted with permission.<sup>20</sup> Copyright 2005, American Chemical Society.

### 1.3 Metal-Organic Frameworks

Metal-organic frameworks (MOFs) are a robust class of intrinsically porous 2D and 3D crystalline materials consisting of metal nodes interconnected by polytopic organic linkers.<sup>25,26</sup> The periodicity observed in single-crystalline MOF materials provides a key advantage in the design of new frameworks, in that X-ray diffraction can be used to obtain atomic-level resolution of metal secondary building unit (SBU) and organic ligand locations.<sup>25–27</sup> Therefore, MOF pore environments can be precisely functionalized and fine-tuned for various applications (Figure 1.2).<sup>28,29</sup> A key motivating factor of MOF research is rooted in their display of exceptionally high surface areas with the theoretical upper limit of MOF surface area being shown to be over twice the current world record.<sup>30,31</sup> Noteworthy surface areas and extended porous channels have led to MOFs excelling as platforms for gas storage and separation, as well as catalysis, drug delivery and sensing.<sup>32–39</sup>

MOFs are simple structures achieved through the repeating assembly of organic ligands and metal SBUs into a periodic net — a far cry from the complexity observed in biological systems.<sup>40</sup> However, due to the nature of metal-coordination bonds, it has been shown that single-crystalline multivariate MOFs (MTV-MOFs) can be synthesized with numerous uniquely functionalized ligands.<sup>41–44</sup> Different variations of MTV-MOF-5 exhibited higher levels H<sub>2</sub> uptake and CO<sub>2</sub>/CO selectivity than MOF-5 with one kind of organic ligand. This was the first indication that MTV-MOFs display properties that are not simply the sum of those observed by MOFs synthesized with the individual organic building blocks.<sup>41</sup> Increasing complexity within the framework coincided with loss of control over discrete MOF composition due to the inability to dictate how the various linkers are distributed throughout individual MOFs. In recent years, the hierarchical structural complexity of MOFs has dramatically expanded.<sup>40,45,46</sup> Early reports of

core-shell MOFs led to the emergence of stratified MOFs (sMOFs), gradient MOFs, and numerous other ‘MOF-on-MOF’ architectures<sup>47–50</sup>

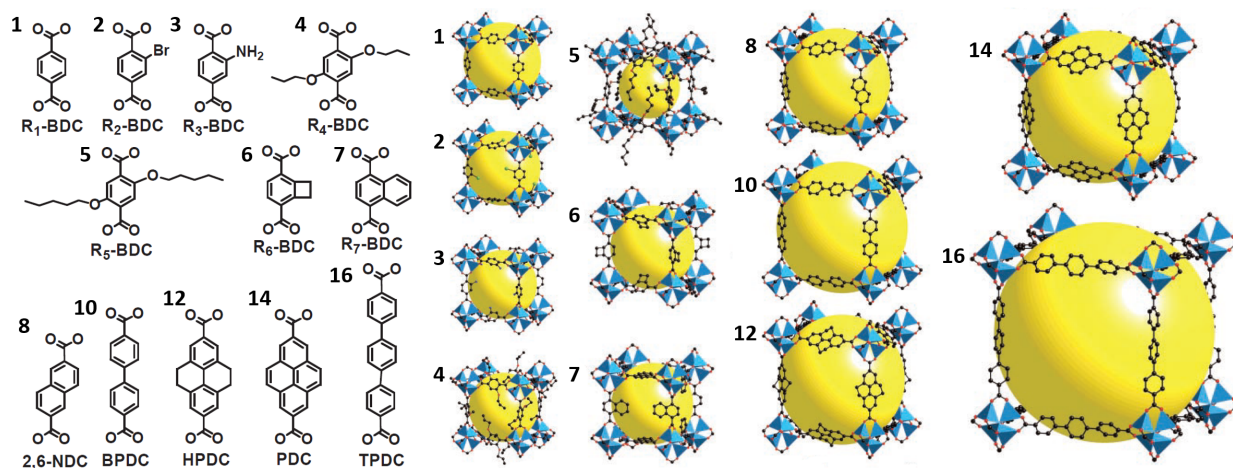


**Figure 1.2** Examples of isorecticular series of MOFs based on MOF-5 depicting tuning of pore environment whilst maintaining cubic framework. Adapted with permission.<sup>28</sup> Copyright 2002, AAAS.

## 1.4 Stratified Metal-Organic Frameworks

Important conceptual advances in MOF design rely on consideration of the MOF itself as a ‘building block’ (c.f. ‘domain building blocks, or DBBs’).<sup>48</sup> DBBs describe distinct compositional or structural regions within a MOF. sMOFs are a subset of MTV-MOFs that contain two or more concentrically organized DBBs. We and others envisage that such hierarchically structured MOF materials can be designed to perform sequences of tasks, reminiscent of complex multicomponent systems, and exhibit functions that rely on synergy between MOF domains. Realizing this vision however, requires precision placement of DBBs with respect to one another and an understanding of synthetic factors that affect domain formation and compositional integrity. sMOF syntheses generally begin with the preparation of a ‘seed’ MOF crystal, which serves as a nucleation center

for growth of subsequent MOF domains. However, the labile nature of metal-linker coordination in MOFs allow for linker exchange reactions to occur concomitantly with shell growth, impeding the achievement of pristine DBBs.<sup>51</sup> Secondary growth reactions with unmitigated linker exchange, can result in a homogeneous mixture of linkers and loss of function observed by sMOF architectures with identical linker compositions.<sup>48,52,53</sup> Furthermore, common characterization techniques cannot accurately locate and differentiate between different organic linkers within a single crystal. Therefore, the development of a reliable method for tracking the migration of linkers throughout a crystal is essential to understanding the competing processes of linker exchange and secondary growth. The work described in this thesis details a systematic effort to more completely define the synthetic parameters that can be tuned to achieve precise control over MTV-MOF composition.

## **2.0 Control of Linker Exchange to Fine-Tune Stratified Metal Organic Framework Composition**

### **2.1 Introduction**

For wide-spread linker exchange to occur, facile diffusion through MOF pores is required.<sup>49,51,53</sup> Therefore, identifying synthetic parameters that can be leveraged to control diffusion is critical for fine-tuning DBB composition in sMOFs. We consider three possible MOF compositions that can result from secondary growth reactions using seed MOFs (Figure 2.1). In the first scenario, shell growth occurs with sufficient mitigation of linker exchange, resulting in a binary ‘core-shell’ sMOF. If linker exchange occurs more rapidly than stratum growth, we expect a statistically random distribution of all linkers. Lastly, we consider the case where stratum growth and linker exchange are equally probable. Over time as the MOF components in the secondary growth solution are depleted, linker exchange will continue to occur and result in loss of compositional integrity between DBBs. However, by closely monitoring the reaction with respect to time, we can isolate MOFs with a gradient distribution of linkers (Figures 3.6 and 3.10). In this work, we use UiO-67 (University of Oslo)<sup>54</sup> as a platform for the systematic study of how linker exchange manifests with respect to ligand sterics, reaction time, and solvent environments in the context of controlling domain composition in sMOFs.

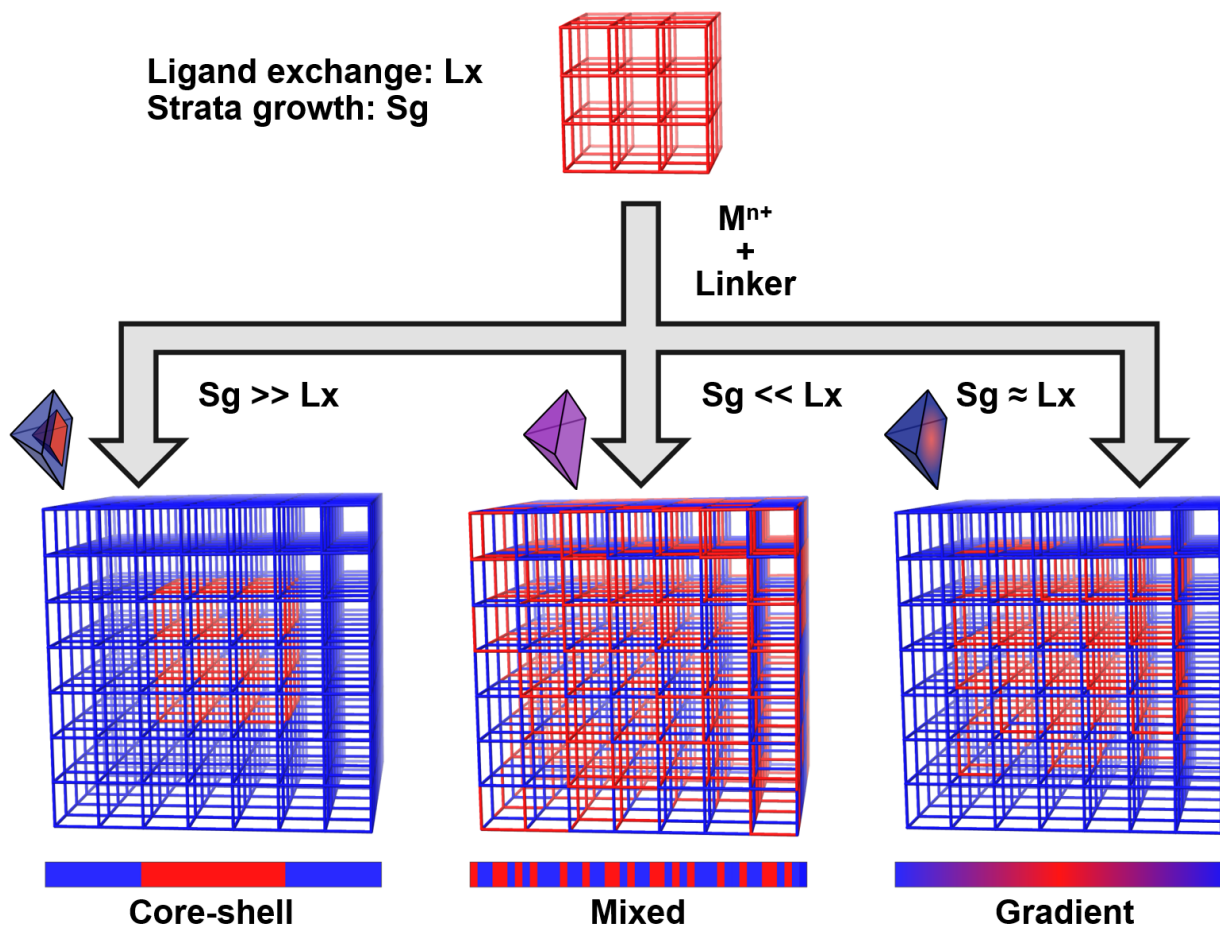


Figure 2.1 Illustrations of possible linker arrangements resulting from secondary growth reaction with 2-D depictions of linker distributions below each example.

## 2.2 Results and Discussion

Specifically, we posit that the extent of linker exchange can be attenuated through incremental increases to the steric bulk of the ligand used for secondary growth. Four linkers that differ significantly in their sterics were designed and synthesized for this study: (I) 1,1'-biphenyl-4,4'-dicarboxylic acid (BPDC), (II) 2-acetamido-1,1'-biphenyl-4,4'-dicarboxylate (N-acetyl-BPDC) (III) 2-((tert-butoxycarbonyl)amino-1,1'-biphenyl-4,4'-dicarboxylate (N-boc-BPDC) and

(IV) (S)-2-(1-(tert-butoxycarbonyl) pyrrolidine-2-carboxamido)-1,1'-biphenyl-4,4'-dicarboxylic acid (proline-boc-BPDC). To quantitatively map linker distribution in sMOFs, a reliable method for tracking the migration of linkers throughout a crystal is necessary. We quantify the extent of linker exchange by coordinating palladium (Pd) metal to 2,2'-bipyridine-5,5'-dicarboxylic acid (BpyDC) within UiO-67 based sMOFs. Specifically, seed crystallites of Bpy-UiO-67(Zr) will be treated with secondary growth solutions containing a Zr source and one of the four shell linkers, all of which do not coordinate Pd, followed by post-synthetic metalation (Figure 2.2).

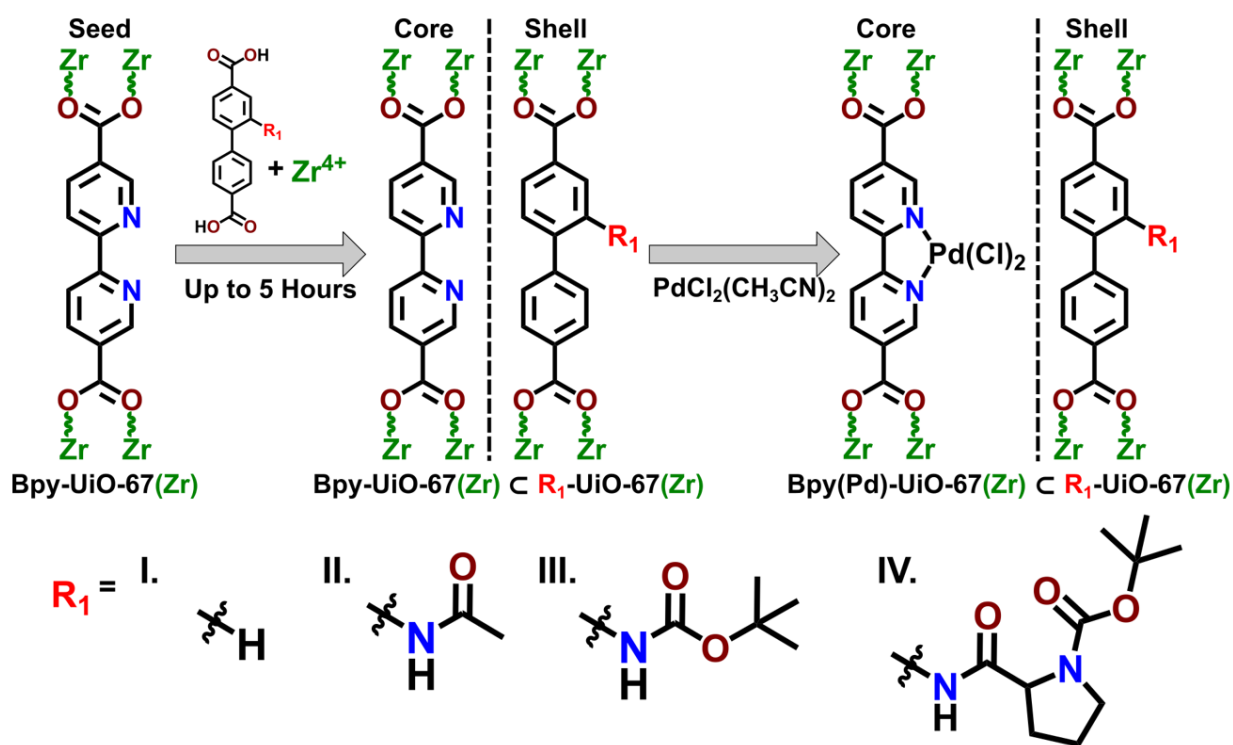


Figure 2.2 Stepwise procedure from seed Bpy-UiO-67(Zr) to post-metalation core-shell Bpy(Pd)-UiO-67(Zr)@R1-UiO-67(Zr) with chemical structures of R1 functional groups illustrated.

We combined  $\text{ZrCl}_4$  and BpyDC to synthesize seed crystals of Bpy-UiO-67(Zr) with a size of  $341 \pm 31$  nm (Figure 3.2). Secondary growth solutions were then prepared using  $\text{Zr}(\text{O}^i\text{Pr})_4$ , acetic acid, dimethylformamide (DMF), and one of the four organic linkers. Seed crystals were then treated with secondary growth solutions and heated to  $65^\circ\text{C}$  for 10 minutes to 48 hours. The

resulting crystals were then washed with DMF, followed by solvent exchange with acetonitrile (ACN). sMOF crystals were then soaked overnight in a solution of bis(acetonitrile)dichloropalladium(II) and copiously washed with ACN to remove any uncoordinated Pd from the framework.

Transmission electron microscopy (TEM) was used to obtain high angle annular dark field (HAADF) images. Core-shell architectures can be visibly observed if Pd is not evenly distributed between strata (Figure 2.3). If no linker exchange occurs, then no Pd should be observed in the shell domain. Meanwhile, unmitigated linker exchange will result in an even distribution of linkers and thus Pd throughout the MOF. When using BPDC for shell growth, (Bpy(Pd)-UiO-67(Zr)<sub>c</sub>(I)-UiO-67(Zr)), strata can be visually detected after 10 and 20 minute reactions. However, after 1 hour of shell growth, no such features are visible (Figure 3.5). A similar, yet slower, trend is observed when synthesizing Bpy(Pd)-UiO-67(Zr)<sub>c</sub>(II)-UiO-67(Zr). Although core-shell architectures are still observable after 2 hours, there is no evidence of stratification after 5 hours (Figure 3.9). When using N-boc-BPDC and proline-boc-BPDC to synthesize Bpy(Pd)-UiO-67(Zr)<sub>c</sub>(III)-UiO-67(Zr) and Bpy(Pd)-UiO-67(Zr)<sub>c</sub>(IV)-UiO-67(Zr) respectively, two distinct domains were observable even after 48 hours of reaction time, at a minimum suggesting that linker exchange had not proceeded to completion in either sample. Qualitatively, this suggests that linker exchange is most rapid in the presence of the least sterically hindered linkers. While HAADF images allow for rapid determination of ligand distribution, they do not provide quantitative data for discerning the amount of linker exchange that has occurred in samples that still have visually observable strata.

In contrast, scanning TEM-energy dispersive X-ray spectroscopy (STEM-EDS) allows for quantitative measure of Pd and zirconium (Zr) at specific points or along lines throughout

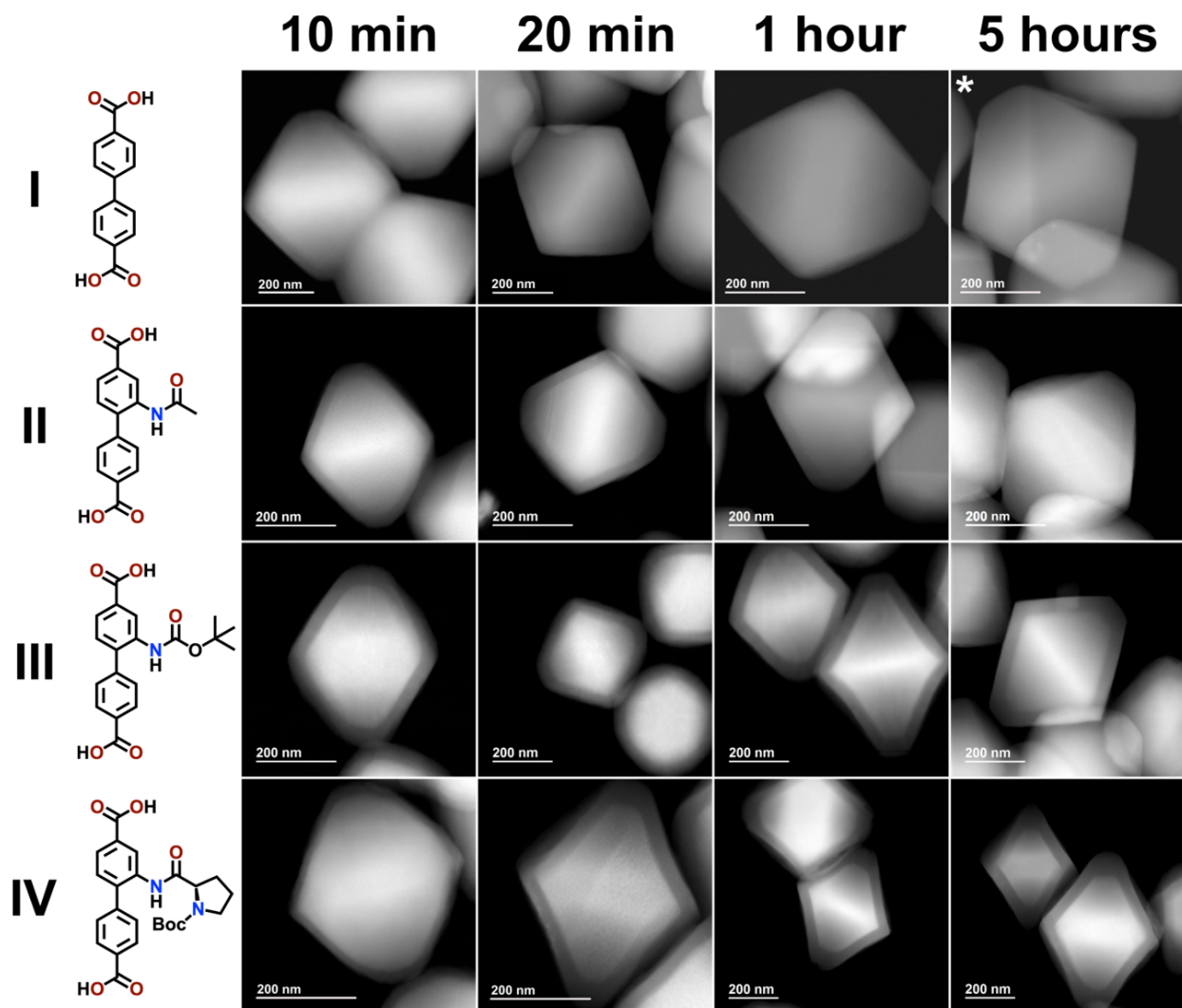


Figure 2.3 HAADF images of Bpy(Pd)-UiO-67(Zr)⊂(I-IV)-UiO-67(Zr) with reaction times between 10 minutes and 5 hours. \*Bpy(Pd)-UiO-67(Zr)⊂(I)-UiO-67(Zr) after 4 hours of reaction.

individual MOF crystals. By measuring the Pd to Zr ratio in the shell strata and tuning reaction time, we can quantitatively monitor linker exchange (Figure 2.4). Mixed linker Bpy-R%-UiO-67 were synthesized with varying ratios of BpyDC and BPDC to test the sensitivity of STEM-EDS at detecting differences in Pd quantity. Exact linker ratios were then determined by nuclear magnetic resonance (NMR) and plotted against measured Pd to Zr ratios. The emerging trendlines for Bpy-R%-UiO-67 with 0 – 50% and 60 - 100% BpyDC both had  $R^2$  values greater than 0.999 (Figure 3.3). This indicates that STEM-EDS can reliably detect incremental changes in linker composition.

STEM-EDS results show that the extent of linker exchange observed during secondary growth can be controlled by tuning linker steric bulk and reaction time. In Bpy(Pd)-UiO-67(Zr)<sub>c</sub>(I)-UiO-67(Zr) and Bpy(Pd)-UiO-67(Zr)<sub>c</sub>(II)-UiO-67(Zr), extended reaction times directly correlate to increases in Pd to Zr ratio in the shell followed by subsequent plateaus after loss of hierarchical structure. These measurements correspond directly to the visual loss of strata observed over time through HAADF. STEM-EDS line-scan data indicates that in both systems, gradient MOF compositions were isolated as intermediates during transitions from core-shell to homogenous linker distributions (Figure 3.6 and Figure 3.10). Sufficient reduction of reaction time resulted in successful synthesis of core-shell Bpy(Pd)-UiO-67(Zr)<sub>c</sub>(I)-UiO-67(Zr) and Bpy(Pd)-UiO-67(Zr)<sub>c</sub>(II)-UiO-67(Zr) with shell Pd to Zr ratios of 0.28 and 0.12, respectively. For context, the lowest Pd to Zr ratio measured in this work was approximately 0.08, achieved after 10 minutes of shell growth using N-boc-BPDC as the linker. We presume the initial ligand exchange is a result of BpyDC linkers located on the surface of seed MOFs being exchanged at the onset of secondary growth. sMOFs synthesized using the more sterically hindered linkers maintained their core-shell architecture for up to 48 hours, presumably because shell linkers were unable to freely diffuse through the pores of the seed MOF (Figure 3.19).

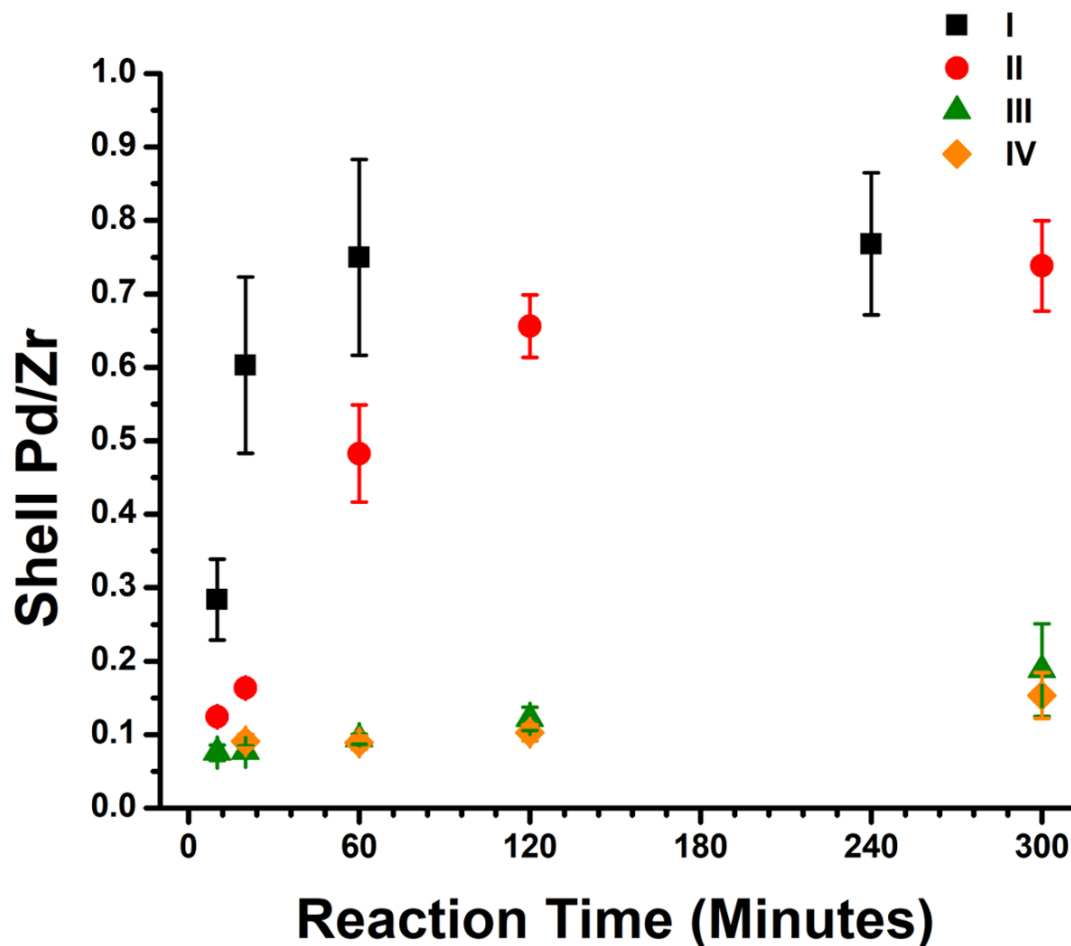
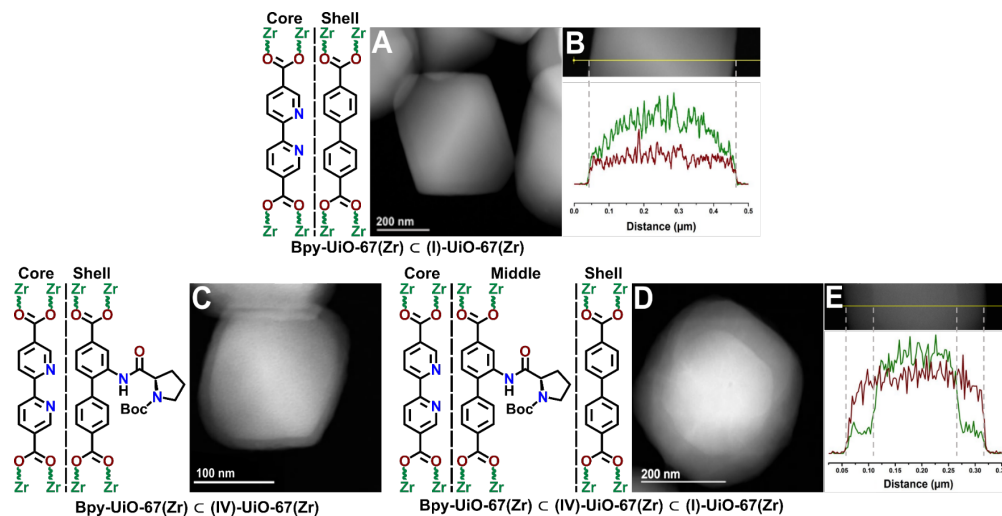


Figure 2.4 Shell Pd to Zr ratio with respect to reaction time in minutes for Bpy(Pd)-UiO-67(Zr) $\subset$ R1-UiO-67(Zr).

We recognize that limiting reaction time to prevent linker exchange is not feasible if the target sMOF has more than two DBBs and requires subsequent secondary growth reactions to synthesize. We hypothesized that sMOFs with three concentric domains with varied linkers can be achieved by using a sterically hindered linker as a ‘gating’ domain between two domains with linkers that otherwise would exchange rapidly. Using this approach, the three-domain sMOF, Bpy(Pd)-UiO-67(Zr) $\subset$ (IV)-UiO-67(Zr) $\subset$ (I)-UiO-67(Zr), was successfully targeted and synthesized (Figure 2.5 D). Secondary growth was first performed for five minutes using proline-boc-BPDC, followed by tertiary growth for twenty minutes with BPDC. STEM-EDS line-scan

data confirmed the mitigation of linker exchange and conservation of sMOF architecture (Figure 2.5 E). In contrast, line-scan data for Bpy(Pd)-UiO-67(Zr) $\subset$ (I)-UiO-67(Zr) synthesized with twenty minutes of secondary growth displayed a gradient distribution of linkers, with a gradual increase in Pd while approaching the core (Figure 2.5 B). This process can theoretically be repeated indefinitely to synthesize sMOFs with various linkers while maintaining pristine DBBs.



**Figure 2.5 (A) HAADF image and (B) EDS line-scan (Zr, red; Pd, green) of Bpy(Pd)-UiO-67(Zr) $\subset$ (I)-UiO-67(Zr) after 20 minutes of shell growth. (C) HAADF image of Bpy(Pd)-UiO-67(Zr) $\subset$ (IV)-UiO-67(Zr) after 5 minutes of shell growth. (D) HAADF image and (E) EDS line-scan of Bpy(Pd)-UiO-67(Zr) $\subset$ (IV)-UiO-67(Zr) $\subset$ (I)-UiO-67(Zr) after 20 minutes of shell growth.**

Many applications of MOFs such as catalysis and drug delivery require exposure to various solvent environments.<sup>38,52</sup> We sought to determine how linker exchange post-synthetically manifests in sMOFs with distinct DBBs by soaking in polar coordinating solvents such as DMF, water, and ACN as well as nonpolar non-coordinating solvents such as hexanes. UiO-67(Zr) $\subset$ (I)-UiO-67(Zr) sMOFs were prepared for solvent stability studies using 10 minutes as the reaction time. BPDC was selected as the shell linker because it has the least steric hinderance of shell linkers in this study and 10 minutes was used for reaction time to minimize the initial Pd to Zr ratio in the shell. No loss of hierarchical structure is observed after soaking at room temperature

in hexanes for 21 days or in DMF and ACN for 13 months (Figure 2.6 A). More stringent solvent environments were then employed in an attempt to induce linker exchange and display post-synthetic control over sMOF composition. Soaking in 85 °C water for 21 hours resulted in visible degradation of the MOF (Figure 3.22) and a decline in crystallinity (Figure 3.23). Soaking in 100 °C DMF, UiO-67(Zr)⊂(I)-UiO-67(Zr) does not exhibit any linker exchange for 24 hours, however an increase of Pd in the shell strata after 48 hours is observed (Figure 3.21). This increase was attributed to the decomposition of DMF which produces formic acid capable of displacing coordinated linkers and facilitating exchange. We then replicated the reaction conditions by soaking UiO-67(Zr)⊂(I)-UiO-67(Zr) in DMF and acetic acid and heating to 65 °C. Complete loss of sMOF composition was observed after 2 hours, with line-scan data confirming a homogenous mixture of linkers (Figure 2.6 B).

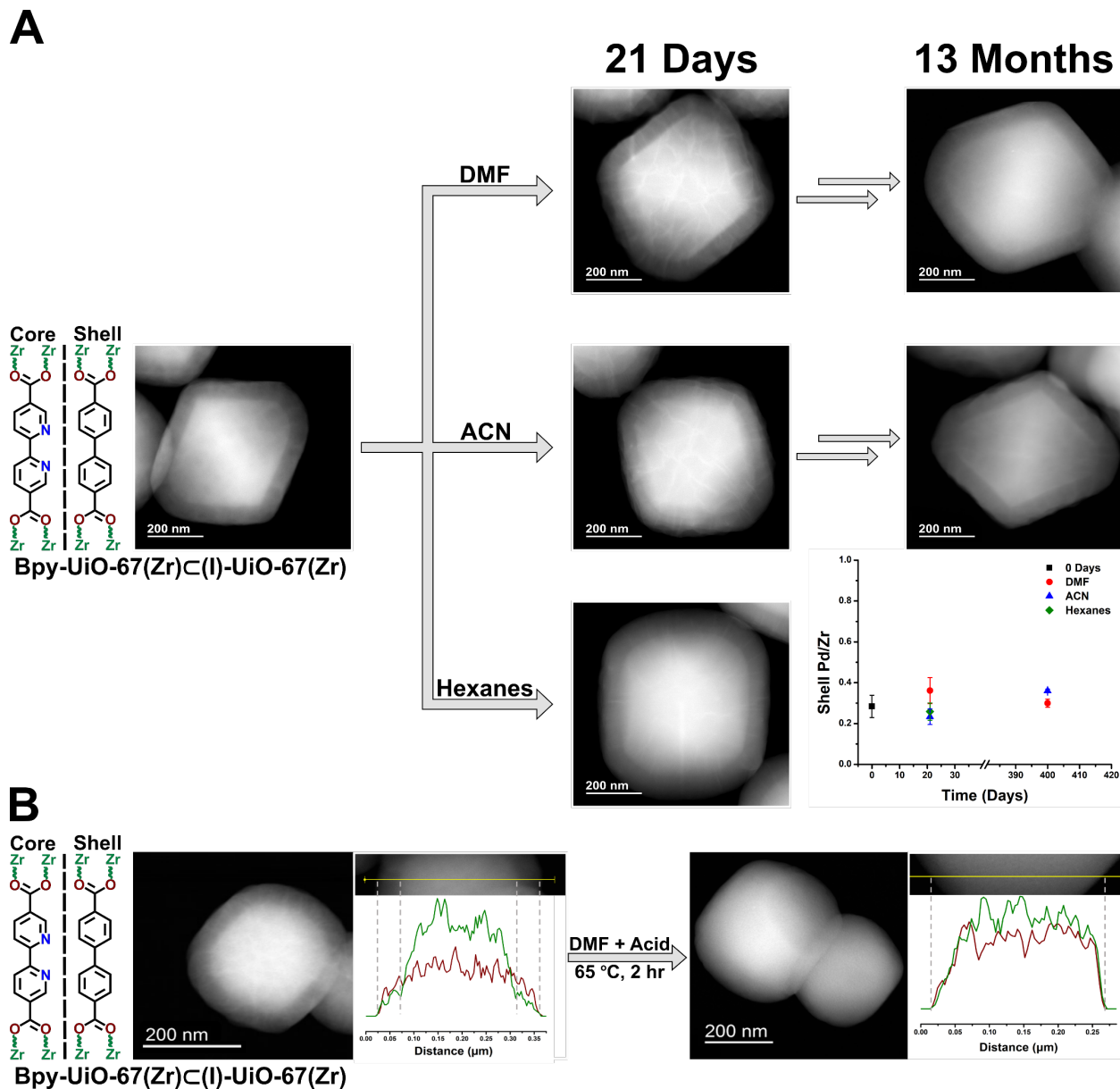


Figure 2.6 (A) HAADF images of Bpy(Pd)-UiO-67(Zr)C(I)-UiO-67(Zr) before and after soaking in DMF, ACN and hexanes for up to 13 months and a plot of the shell Pd to Zr ratio over time and (B) HAADF images and EDS line-scans (Zr, red; Pd, green) of Bpy(Pd)-UiO-67(Zr)C(I)-UiO-67(Zr) before and after soaking in DMF and acetic acid at 65 °C for two hours.

## 2.3 Conclusion

Control over composition down to the placement of linkers in distinct DBBs is fundamental to expanding the functional diversity of sMOFs. We have shown that linker exchange can be controlled and mitigated during synthesis with incremental changes in linker sterics and reaction time. By taking advantage of these two conditions, well-defined DBBs were targeted and synthesized while maintaining hierarchical complexity. This strategy has also revealed a method for achieving gradient MOF architectures by monitoring secondary growth reactions to selectively allow linker exchange to occur and terminating the reaction before linkers are homogeneously mixed. sMOFs exhibited exceptional stability in various solvent environments, maintaining their hierarchical structure after 13 months in DMF and ACN at room temperature. More stringent solvent environments were successfully employed to post-synthetically induce linker exchange. Our work in investigating the effects of key synthetic parameters on linker exchange has broadened the understanding of sMOF synthesis and compositional integrity by implementing new techniques for characterization of linker distribution and expanding the catalog of achievable hierarchical architectures.

## 3.0 Experimental Section

### 3.1 General Methods

Powder X-ray diffraction patterns were collected using a Bruker AXS D8 Discover powder diffractometer at 40 kV, 40 mA for Cu K $\alpha$  ( $\lambda = 1.5406 \text{ \AA}$ ) with a scan speed of 0.20 sec/step from 3.5 to 45° at a step size of 0.02°. The EVA program from the Bruker Powder Analysis Software package was used to perform background correction. Simulated powder patterns were calculated using Mercury 3.8 based on MOF crystal structures accepted by the Cambridge Crystallographic Data Centre.

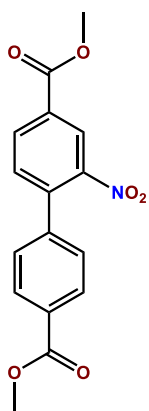
<sup>1</sup>H NMR spectra were obtained using Bruker Avance III 300/400/500 MHz spectrometers. Chemical shifts are presented in parts per million (ppm) using the residual solvent peak (CDCl<sub>3</sub>, DMSO-d<sub>6</sub>, or D<sub>2</sub>O) as references. MOF samples were digested with DMSO-d<sub>6</sub> and a small amount of hydrofluoric acid 48%, or K<sub>3</sub>PO<sub>4</sub> and D<sub>2</sub>O.

Transmission electron microscopy (TEM) images of MOF crystallites were collected on a FEI Morgagni 268 operated at 80 kV with an AMT side mount CCD camera system. High angle annular dark field (HAADF) imaging and scanning transmission electron microscopy-energy dispersive X-ray spectroscopy (STEM-EDS) studies were conducted on a JEOL JEM-2100F. The STEM-EDS data was collected using 1024 channels from 0 to 20 keV. Zirconium point spectrum and line-scans were obtained using the Zr K $\alpha$ 1 line intensity at 15.7 keV. Palladium point spectrum and line-scans were obtained using the Pd L $\alpha$ 1 line intensity at 2.8 keV. Chlorine point spectrum were obtained using the Cl K $\alpha$ 1 line intensity at 2.6 keV. Samples were dispersed in ethanol or

acetonitrile (ACN) and drop cast on TEM grids (Ted Pella Inc 200 mesh carbon film copper grids). The TEM grids were dried under ambient conditions before TEM and STEM-EDS analyses.

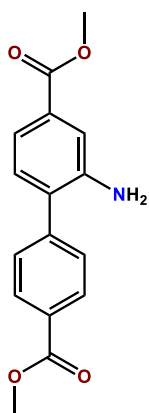
### 3.2 Synthesis and Characterization of Organic Linkers

#### 3.2.1 Dimethyl 2-nitro-1,1'-biphenyl-4,4'-dicarboxylate (1)



Compound **1** was synthesized according to literature conditions.<sup>55</sup>

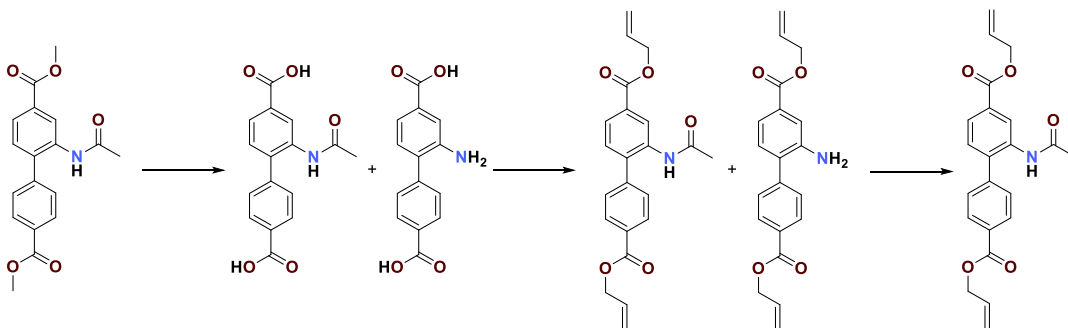
#### 3.2.2 Dimethyl 2-amino-1,1'-biphenyl-4,4'-dicarboxylate (2)



Compound **2** was synthesized according to literature conditions.<sup>48</sup>

### 3.2.3 2-acetamido-1,1'-biphenyl-4,4'-dicarboxylate (3)

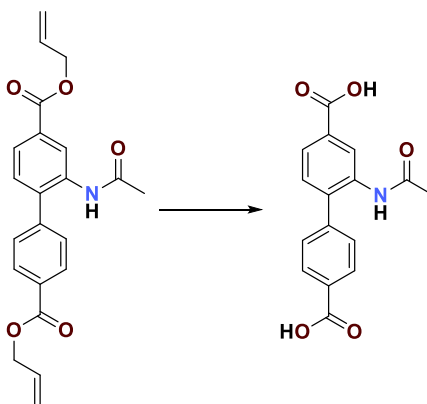
To a solution of compound **2** (856 mg, 3 mmol) in anhydrous dichloromethane (20 mL) was added trimethylamine (500  $\mu$ L, 3.6 mmol), and acetyl chloride (257  $\mu$ L, 3.6 mmol) dropwise at 0  $^{\circ}$ C. The mixture was stirred and monitored at room temperature until complete as indicated by TLC. The reaction was quenched with water (10 mL). The organic phase and aqueous phase were separated. The aqueous phase was extracted with dichloromethane three times. The organic phases were combined and washed with water and brine and dried over sodium sulfate. The organic phase was concentrated in vacuo. The residual was purified via silica gel chromatography (Ethyl acetate:Hexanes 1:1) to yield 750 mg of dimethyl 2-acetamido-1,1'-biphenyl-4,4'-dicarboxylate product.  $^1\text{H NMR}$  (300 MHz,  $\text{CDCl}_3$ )  $\delta$  8.82 (s, 1H), 8.17 (m, 2H), 7.91 (dd,  $J = 7.3, 1.2$  Hz, 1H), 7.47 (m, 2H), 7.34 (d,  $J = 8.0$  Hz, 1H), 7.00 (d,  $J = 1.2$  Hz, 1H), 3.97 (s, 3H), 3.92 (s, 3H), 2.04 (s, 3H).



Dimethyl 2-acetamido-1,1'-biphenyl-4,4'-dicarboxylate (750 mg, 2.3 mmol) was dissolved in a 1:1 mixture of THF/MeOH (40 mL). To the solution of dimethyl 2-acetamido-1,1'-biphenyl-4,4'-dicarboxylate, was added 1 M NaOH aqueous solution (23 mL). The reaction mixture was stirred and refluxed for 24 hours and then concentrated in vacuo to remove THF and MeOH. The aqueous residue was then acidified with 1 M HCl solution until the pH of solution reached  $\sim 2$  and a yellow slurry formed. The slurry was stirred for 30 min. After vacuum filtration, solid precipitate

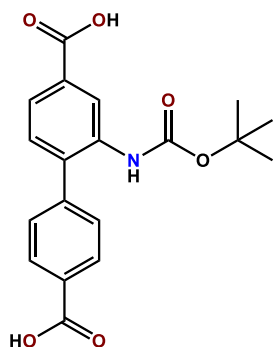
was collected and washed with water (4x, 20 mL for each time). The solid product was dried under vacuum.  $^1\text{H}$  NMR indicated that the product was a mixture of 2-acetamido-1,1'-biphenyl-4,4'-dicarboxylic acid and 2-amino-1,1'-biphenyl-4,4'-dicarboxylic acid.

To the mixture of 2-acetamido-1,1'-biphenyl-4,4'-dicarboxylic acid and 2-amino-1,1'-biphenyl-4,4'-dicarboxylic acid (520 mg, 2 mmol) obtained above, was added potassium carbonate (662 mg, 4.8 mmol) and dimethyl formamide (DMF) (5 mL). Allyl bromide (415  $\mu\text{L}$ , 4.8 mmol) was added dropwise at room temperature. The reaction was stirred at room temperature for 24 hours. After addition of water (10 mL), the reaction mixture was extracted with dichloromethane (3x, 20 mL for each time). the combined organic phase was then washed with brine, dried over sodium sulfate and concentrated in vacuo. The product was dissolved in 10 mL dichloromethane, to which trimethylamine (280  $\mu\text{L}$ , 2 mmol) and acetyl chloride (146  $\mu\text{L}$ , 2 mmol) was added at 0  $^\circ\text{C}$  with stirring. The mixture was stirred at room temperature for 24 h, and then quenched with water (10 mL). The organic phase and aqueous phase were separated. The aqueous phase was extracted with dichloromethane three times. The combined organic phase was washed with water and brine, dried over sodium sulfate and concentrated in vacuo. The residual was purified via silica gel chromatography to obtain 600 mg pure diallyl 2-acetamido-1,1'-biphenyl-4,4'-dicarboxylate product.  $^1\text{H}$  NMR (400 MHz,  $\text{CDCl}_3$ )  $\delta$  8.84 (s, 1H), 8.19 (m, 2H), 7.91 (dd,  $J = 7.9, 0.9$  Hz, 1H), 7.47 (m, 2H), 7.34 (d,  $J = 8.0$  Hz, 1H), 7.03 (d,  $J = 0.9$  Hz, 1H), 6.06 (m, 2H), 5.46 (m, 2H), 5.31 (m, 2H), 4.86 (m, 4H), 2.04 (s, 3H).



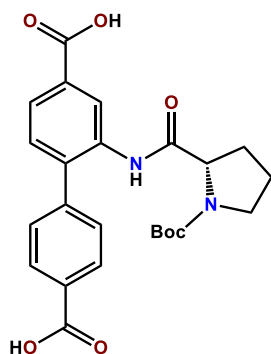
Diallyl 2-acetamido-1,1'-biphenyl-4,4'-dicarboxylate (600 mg, 1.5 mmol) and anhydrous tetrahydrofuran (5 mL) was charged to a 20 mL vial equipped with a septum. The solution was purged with argon flowed for 15 min and protected under argon atmosphere with a balloon. To the THF solution was added tetrakis(triphenylphosphine)palladium (173 mg) in degassed THF (3 mL), and morpholine (260  $\mu$ L, 3 mmol) dropwise. The reaction mixture was stirred at room temperature for 3 h and concentrated in vacuo. To the residual was added ethyl acetate and sodium bicarbonate aqueous solution. The organic and aqueous phases were separated. The organic phase was extracted with sodium bicarbonate two times. The combined aqueous phase was acidified using 1 M HCl solution until pH of the solution reached  $\sim$ 2 and a slurry formed. After vacuum filtration, solid product of 2-acetamido-1,1'-biphenyl-4,4'-dicarboxylic acid was collected, washed with water (4x, 20 mL for each time), and dried under vacuum.  $^1\text{H}$  NMR (500 MHz, DMSO- $d_6$ )  $\delta$  13.07 (s, 2H), 9.48 (s, 1H), 8.07 (d,  $J$  = 0.9 Hz, 1H), 8.02 (m, 2H), 7.84 (dd,  $J$  = 7.9, 0.9 Hz, 1H), 7.53 (m, 2H), 7.48 (d,  $J$  = 8.0 Hz, 1H), 1.91 (s, 3H).

### 3.2.4 2-(tert-butoxycarbonylamino)-1,1'-biphenyl-4,4'-dicarboxylate (4)



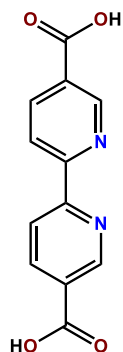
Compound 4 was synthesized according to literature conditions.<sup>56</sup>

### 3.2.5 (S)-2-(1-(tert-butoxycarbonyl) pyrrolidine-2-carboxamido)-1,1'-biphenyl-4,4'-dicarboxylic acid (5)



Compound 5 was synthesized according to literature conditions.<sup>57</sup>

### 3.2.6 2,2'-Bipyridine-5,5'-dicarboxylic acid (6)



Compound 6 was synthesized according to literature conditions.<sup>58</sup>

### 3.3 Synthesis and Characterization of Metal Organic Frameworks

#### 3.3.1 Synthesis of Bpy-UiO-67(Zr) seed crystallites

Bpy-UiO-67(Zr) seed crystallites were synthesized using one of the following conditions.

**Condition I:** To a 20 mL Pyrex vial, ZrCl<sub>4</sub> (9.8 mg, 0.04 mmol), DMF (10 mL), CH<sub>3</sub>COOH (0.5 mL) and H<sub>2</sub>-BpyDC (9.3 mg, 0.04 mmol) were added sequentially. After sonication for 5 min, the vial was placed in a 100 °C oven for 24 hours. The reaction suspension was then centrifuged at 10,000 rpm for 3 min to obtain white precipitate. The precipitate was washed with fresh DMF (16 mL, 4x) and dispersed in DMF (5 mL). An aliquot of the suspension is then removed, washed with ACN (4 mL, 4x), dried under vacuum and weighed. The mass and formula unit of UiO-67(Zr) was used to calculate an effective concentration of the suspension in mmol UiO-67(Zr)/mL to be used for shell growth reactions.

**Condition II:** To a 40 mL Pyrex vial, ZrCl<sub>4</sub> (29.4 mg, 0.12 mmol), DMF (30 mL), CH<sub>3</sub>COOH (1.5 mL) and H<sub>2</sub>-BpyDC (27.9 mg, 0.12 mmol) were added sequentially. After sonication for 5 min, the vial was placed in a 100 °C oven for 16 hours. The reaction suspension was then centrifuged at 10,000 rpm for 3 min to obtain white precipitate. The precipitate was washed with fresh DMF (16 mL, 4x) and dispersed in DMF (5 mL). An aliquot of the suspension is then removed, washed with ACN (4 mL, 4x), dried under vacuum and weighed. The mass and formula unit of UiO-67(Zr) is used to calculate an effective concentration of the suspension in mmol UiO-67(Zr)/mL to be used for shell growth reactions.

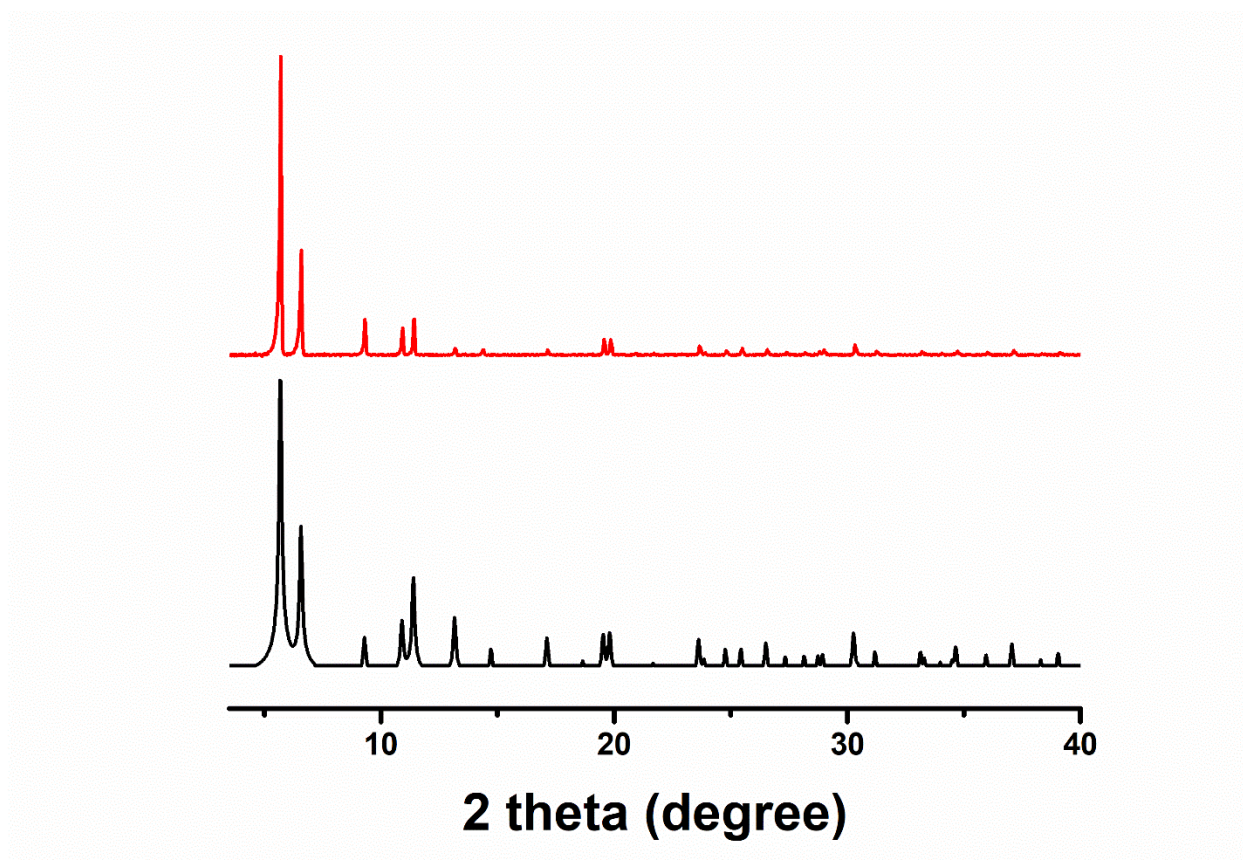


Figure 3.1 Simulated PXR D pattern of UiO-67(Zr) (black) and experimental PXR D of as synthesized Bpy-UiO-67(Zr) seed crystallites (red).

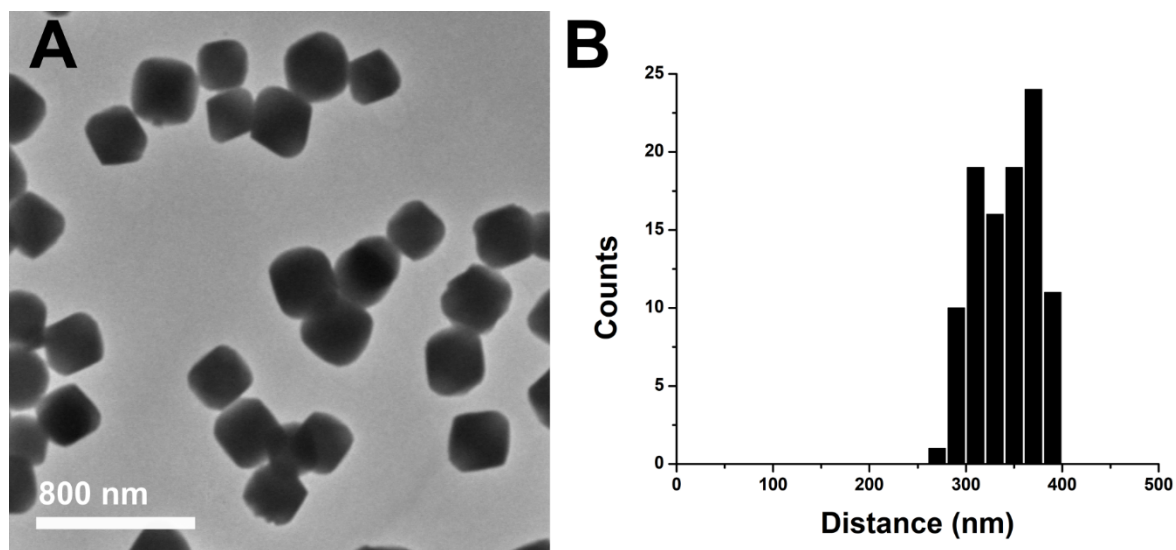


Figure 3.2 TEM image (A) and size distribution (B) of Bpy-UiO-67(Zr) seed crystallites having an average diameter of  $341 \pm 31$  nm ( $n=100$  counts).

### 3.3.2 Calibration of EDS for palladium detection

Synthesis of Bpy-R%-UiO-67(Zr) (R = 0, 10, 25, 40, 50, 60, 75, 90, 100). To a 40 mL Pyrex vial ZrCl<sub>4</sub> (29.4 mg, 0.12 mmol), DMF (30 mL), CH<sub>3</sub>COOH (1.5 mL), H<sub>2</sub>-BpyDC (27.7, 24.9, 20.8, 16.6, 13.9, 11.1, 6.9, 2.8, 0 mg respectively), and H<sub>2</sub>-BPDC (0, 2.8, 7.0, 11.2, 14.0, 16.7, 20.9, 25.1, 27.9 mg respectively) were added sequentially. After sonication for 5 min, the vial was placed in a 100 °C oven for 16 hours. The reaction suspension was then centrifuged at 10,000 rpm for 3 min to obtain white precipitate. The precipitate was washed with fresh DMF (16 mL, 4x) and ACN (4 mL, 4x) and then soaked in an ACN solution of bis(acetonitrile)dichloropalladium(II) overnight followed by an ACN wash (6 x 6 mL) to remove excess uncoordinated palladium.

Linker ratios for each sample were first quantified using NMR. The palladium to zirconium ratio was then collected by taking STEM-EDS point spectra throughout individual MOFs. The calculated Pd to Zr ratios were then plotted against the percentage of all linkers that are H<sub>2</sub>-BpyDC. Different trends were observed for samples with 50% or less H<sub>2</sub>-BpyDC and greater than 50% H<sub>2</sub>-BpyDC, resulting in two trendlines being generated.

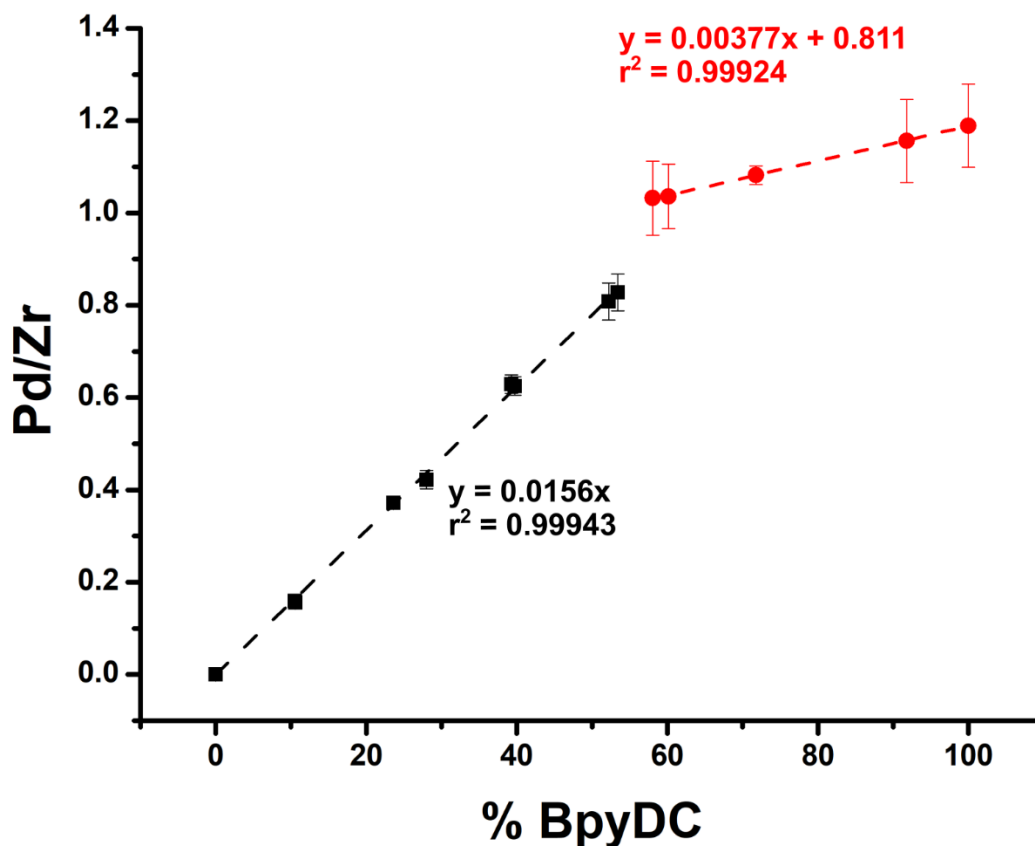
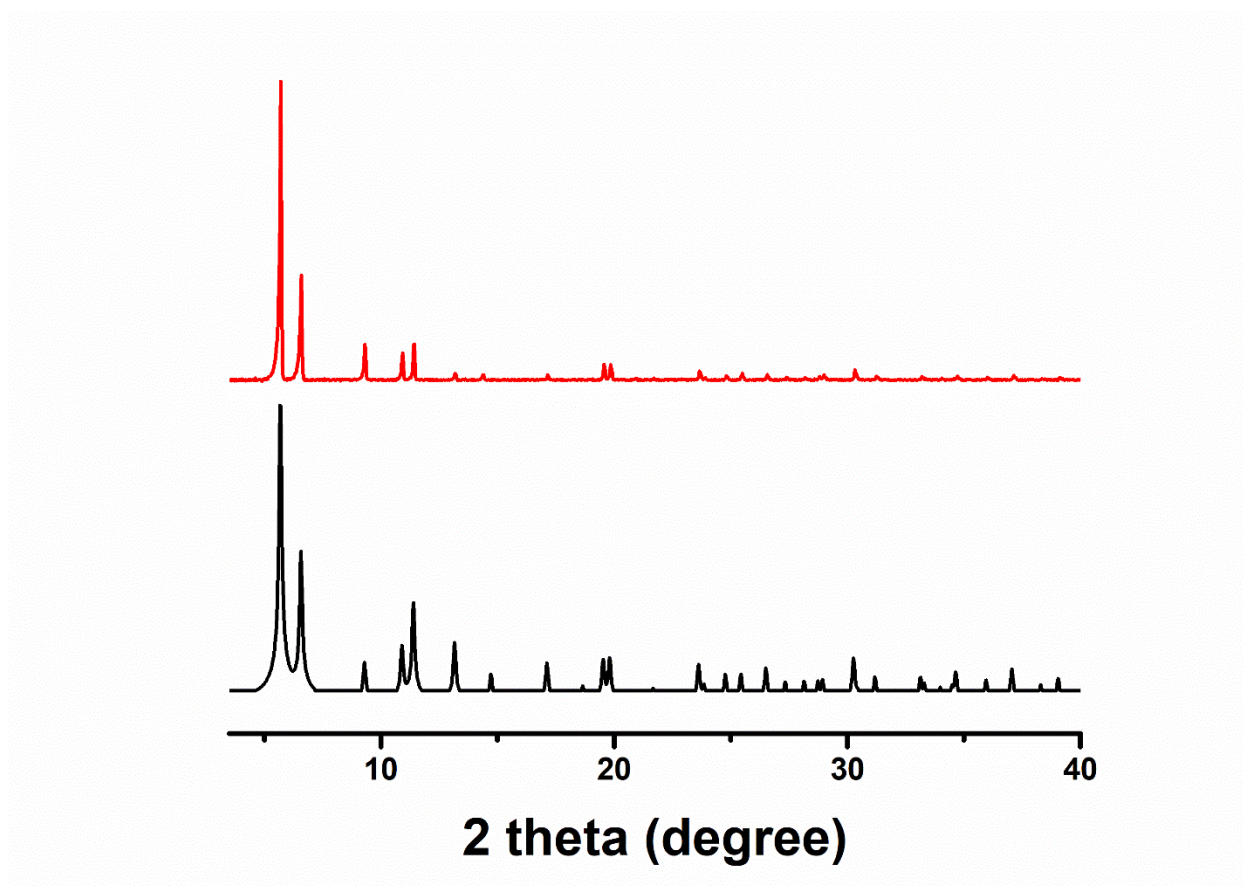


Figure 3.3 Palladium to zirconium ratios of mixed linker Bpy-R%-UiO-67(Zr) MOFs with trendlines made for R% 0 – 50% (black) and R% 60 – 100% (red).

### 3.3.3 Synthesis of Bpy-UiO-67(Zr) $\subset$ UiO-67(Zr) sMOF

0.4 M solution of  $Zr(O^iPr)_4$  in  $CH_3COOH$  was prepared by mixing  $Zr(O^iPr)_4$  70 wt. % in n-propanol (187.2 mg, 0.4 mmol) with  $CH_3COOH$  (1 mL). A 0.02 M solution of  $H_2$ -BPDC was prepared by heating a mixture of  $H_2$ -BPDC (19.4 mg, 0.08 mmol) and DMF (4 mL) on a stir plate at 150 °C until complete dissolution. To a 20 mL Pyrex vial,  $CH_3COOH$  (0.3 mL), 0.4 M  $Zr(O^iPr)_4$  solution in  $CH_3COOH$  (0.05 mL, 0.02 mmol), DMF (4 - X mL), 0.02 M  $H_2$ -BPDC solution (1 mL, 0.02 mmol) and suspension of Bpy-UiO-67(Zr) in DMF (X mL, 0.0191 mmol) were added

sequentially. The mixture was vortexed for 10 seconds and stirred at 120 rpm in a 65 °C oil bath for 10, 20, 60, or 240 minutes. Suspensions were then centrifuged at 10,000 rpm for 3 minutes to obtain a white precipitate, Bpy-UiO-67(Zr)  $\subset$  UiO-67(Zr). The precipitate was washed with fresh DMF (4 mL, 4x), ACN (4 mL, 4x) and then soaked in an ACN solution of bis(acetonitrile)dichloropalladium(II) overnight. A subsequent ACN wash (6 x 6 mL) was conducted to remove excess uncoordinated palladium.



**Figure 3.4** Simulated PXRD pattern of UiO-67(Zr) (black) and experimental PXRD of as synthesized Bpy-UiO-67(Zr)  $\subset$  UiO-67(Zr) sMOF (red).

**Table 3.1 Shell palladium to zirconium ratio calculated using STEM-EDS for Bpy(Pd)-UiO-67(Zr)  $\subset$  UiO-67(Zr) synthesized with different reaction times.**

<b>Reaction Time (min)</b>	<b>Shell Pd/Zr</b>
10	$0.28 \pm 0.06$
20	$0.60 \pm 0.12$
60	$0.75 \pm 0.13$
240	$0.77 \pm 0.10$

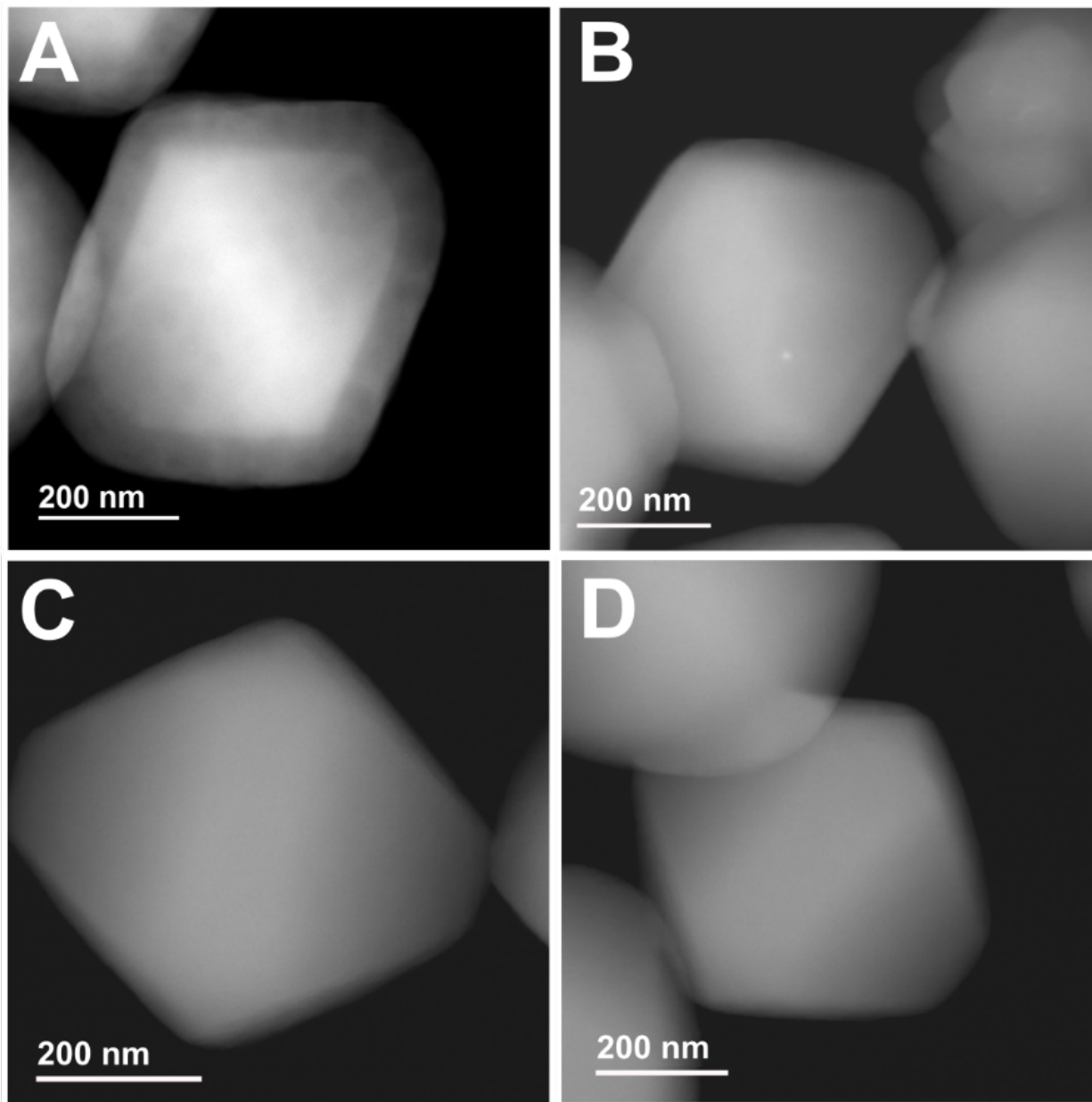


**Figure 3.5 HAADF TEM images of Bpy(Pd)-UiO-67(Zr)  $\subset$  UiO-67(Zr) sMOFs after (A) 10 minutes, (B) 20 minutes, (C) 60 minutes, and (D) 4 hours of reaction time.**

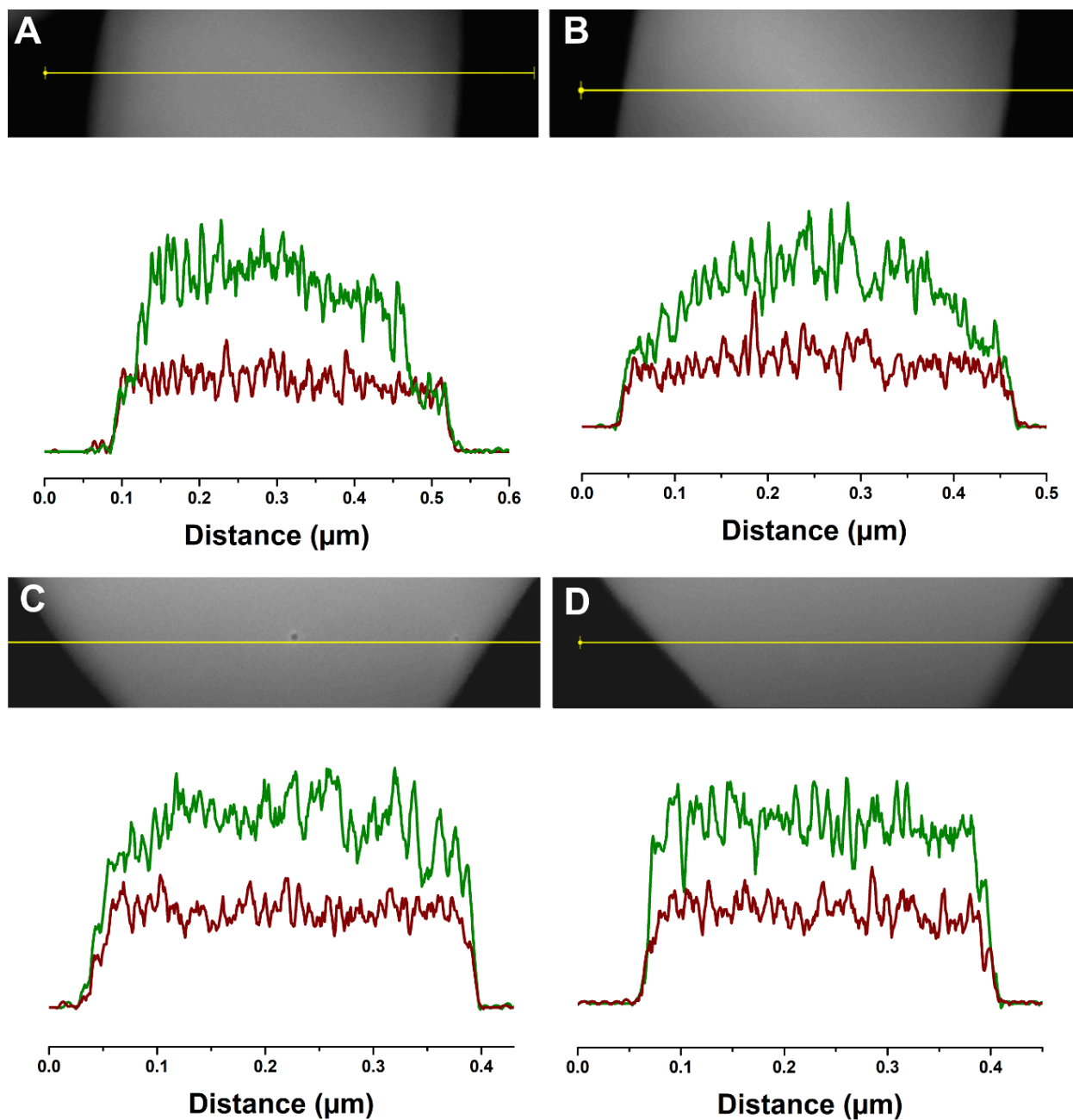


Figure 3.6 STEM-EDS line-scans of Bpy(Pd)-UiO-67(Zr)  $\subset$  UiO-67(Zr) sMOFs (Zr, red; Pd, green) after (A) 10 minutes, (B) 20 minutes, (C) 60 minutes, and (D) 4 hours of reaction time.

### 3.3.4 Synthesis of Bpy-UiO-67(Zr) ⊂ N-Acetyl-UiO-67(Zr) sMOF

0.4 M solution of  $Zr(O^iPr)_4$  in  $CH_3COOH$  was prepared by mixing  $Zr(O^iPr)_4$  70 wt. % in n-propanol (187.2 mg, 0.4 mmol) with  $CH_3COOH$  (1 mL). A 0.02 M solution of 2-acetamido-BPDC was prepared by adding 2-acetamido-BPDC (23.9 mg, 0.08 mmol) to DMF (4 mL) and sonicated until complete dissolution. To a 20 mL Pyrex vial,  $CH_3COOH$  (0.25 mL), 0.4 M  $Zr(O^iPr)_4$  solution in  $CH_3COOH$  (0.05 mL, 0.02 mmol), DMF (4 – X mL), 0.02 M 2-acetamido-BPDC solution (1 mL, 0.02 mmol) and DMF suspension of Bpy-UiO-67(Zr) (X mL, 0.0191 mmol) were added sequentially. The mixture was vortexed for 10 seconds and stirred at 120 rpm in a 65 °C oil bath for 10, 20, 60, 120 or 300 minutes. Suspensions were then centrifuged at 10,000 rpm for 3 minutes obtain a white precipitate, Bpy-UiO-67(Zr) ⊂ N-Acetyl-UiO-67(Zr). The precipitate was washed with fresh DMF (4 mL, 4x) and ACN (4 mL, 4x) and then soaked in an ACN solution of bis(acetonitrile)dichloropalladium(II) overnight. A subsequent ACN wash (6 x 6 mL) was conducted to remove excess uncoordinated palladium.

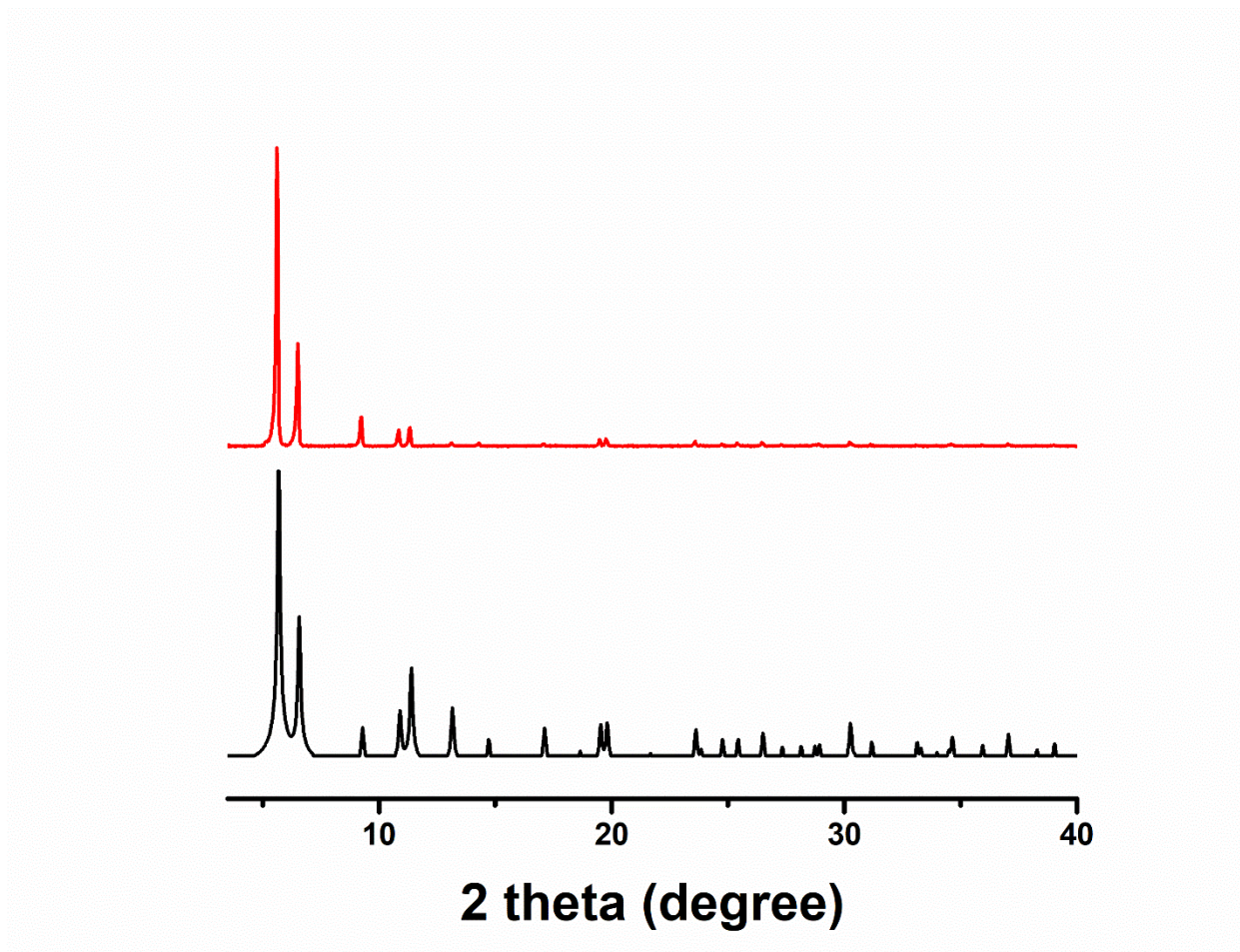
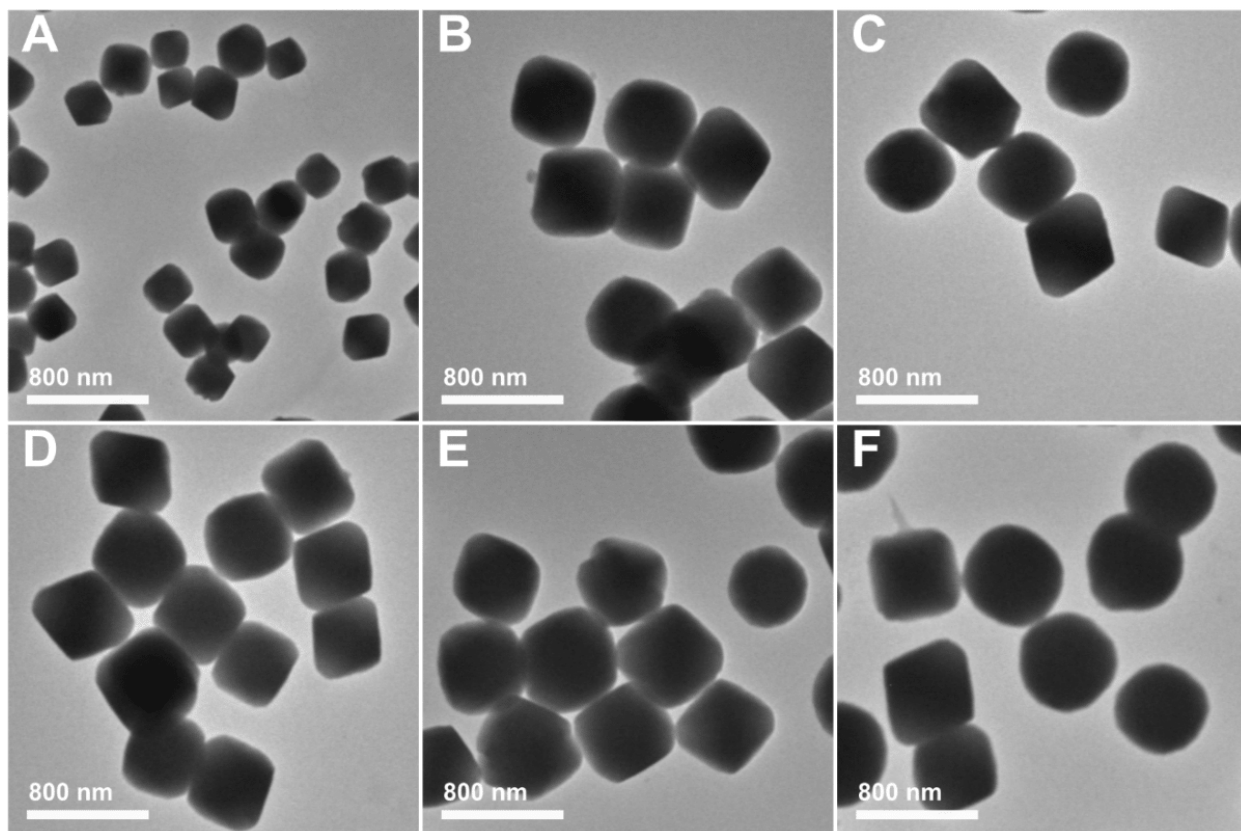


Figure 3.7 Simulated PXRD pattern of UiO-67(Zr) (black) and experimental PXRD of as synthesized Bpy-UiO-67(Zr)  $\subset$  N-Acetyl-UiO-67(Zr) sMOF(red).



**Figure 3.8** TEM images of (A) Bpy-UiO-67(Zr) seed crystallites and Bpy-UiO-67(Zr)  $\subset$  N-Acetyl-UiO-67(Zr) sMOFs after (B) 10 minutes, (C) 20 minutes, (D) 60 minutes, (E) 2 hours, and (F) 5 hours of reaction time.

**Table 3.2** Shell palladium to zirconium ratio calculated using STEM-EDS for Bpy(Pd)-UiO-67(Zr)  $\subset$  N-Acetyl-UiO-67(Zr) synthesized with different reaction times.

Reaction Time (min)	Shell Pd/Zr
10	$0.12 \pm 0.01$
20	$0.16 \pm 0.01$
60	$0.48 \pm 0.07$
120	$0.66 \pm 0.04$
300	$0.74 \pm 0.06$

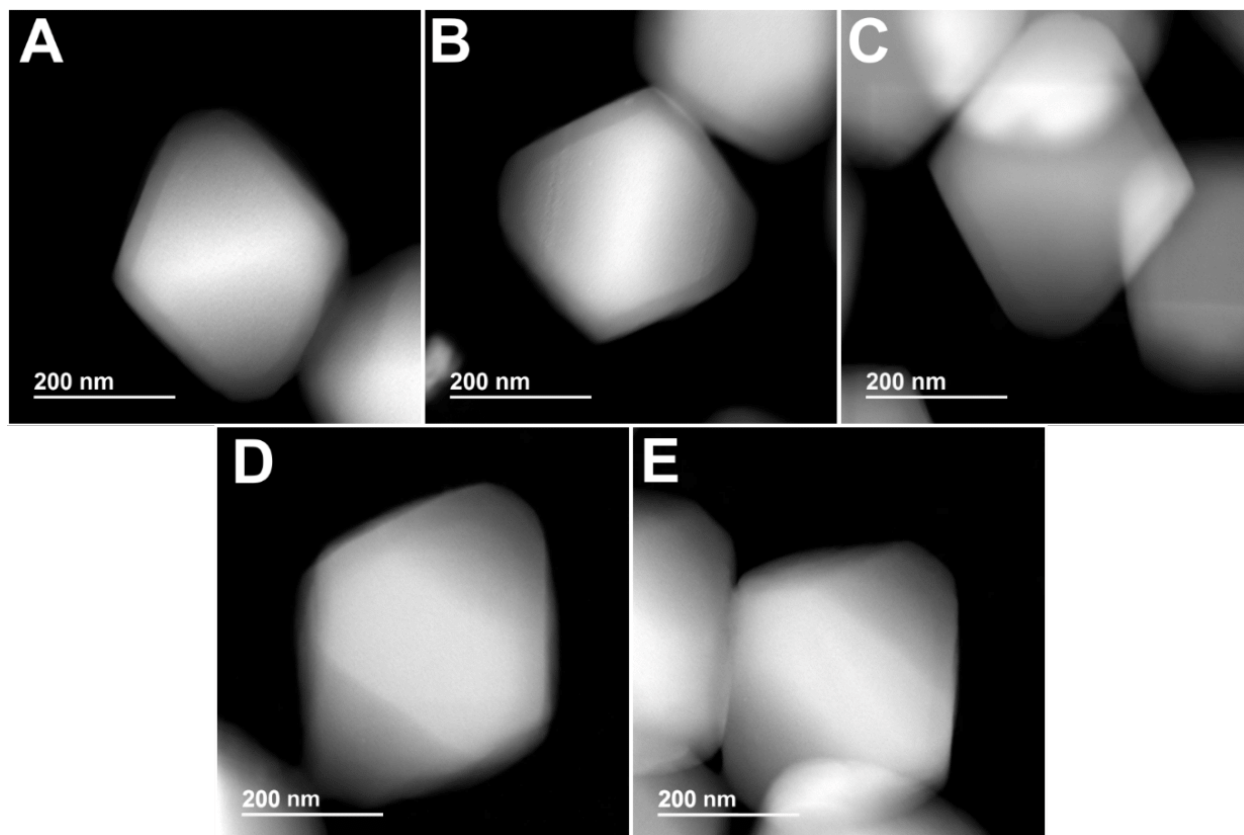


**Figure 3.9** HAADF TEM images of Bpy(Pd)-UiO-67(Zr)  $\subset$  N-Acetyl-UiO-67(Zr) sMOFs after (A) 10 minutes, (B) 20 minutes, (C) 60 minutes, (D) 2 hours, and (E) 5 hours of reaction time.

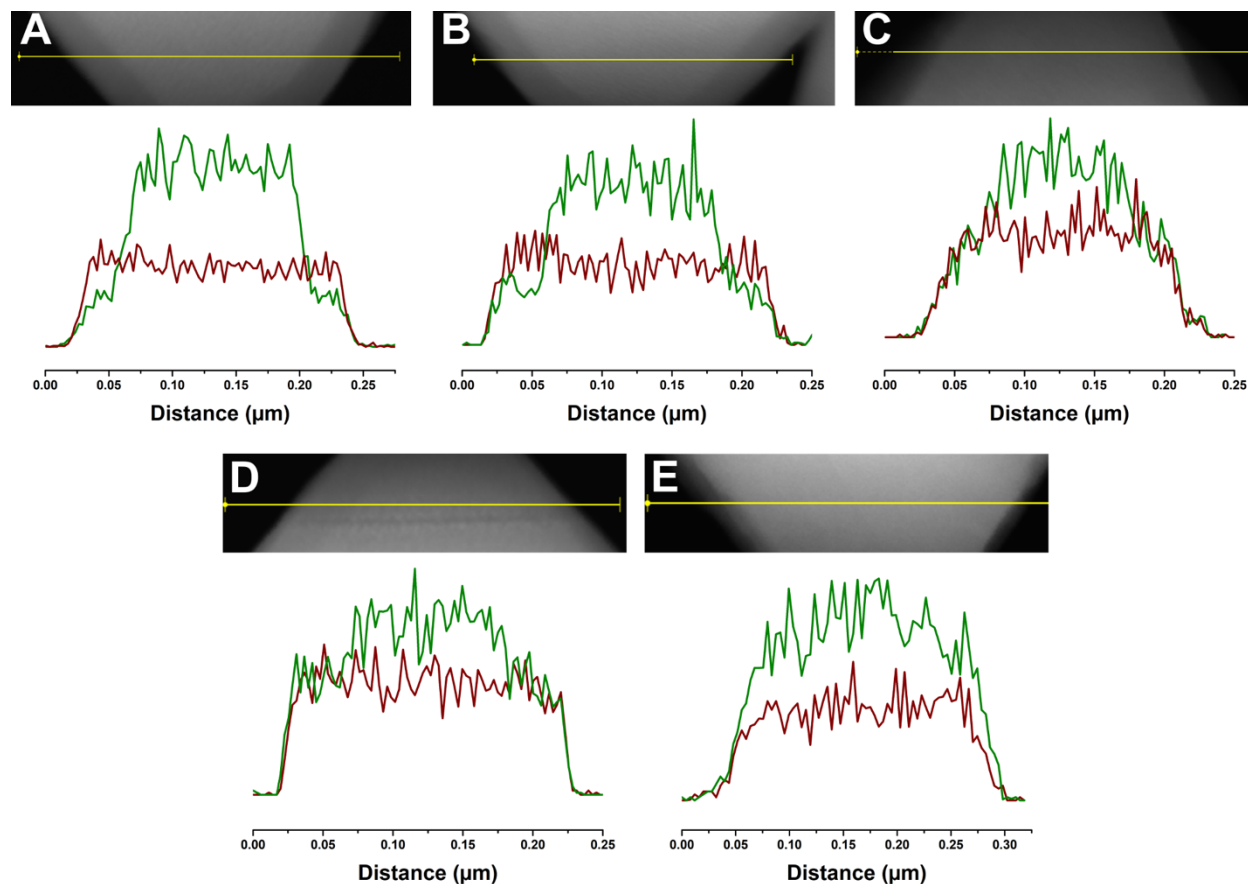


**Figure 3.10** STEM-EDS line-scans of Bpy(Pd)-UiO-67(Zr) @ N-Acetyl-UiO-67(Zr) sMOFs (Zr, red; Pd, green) after (A) 10 minutes, (B) 20 minutes, (C) 60 minutes, (D) 2 hours, and (E) 5 hours of reaction time.

### 3.3.5 Synthesis of Bpy-UiO-67(Zr) @ N-boc-UiO-67(Zr) sMOF

0.4 M solution of  $Zr(O^iPr)_4$  in  $CH_3COOH$  was prepared by mixing  $Zr(O^iPr)_4$  70 wt. % in n-propanol (187.2 mg, 0.4 mmol) with  $CH_3COOH$  (1 mL). A 0.02 M solution of 2-(tert-butoxycarbonylamino)-BPDC (N-boc-BPDC) in DMF was prepared by adding N-boc-BPDC (28.6 mg, 0.08 mmol) to DMF (4 mL) and sonicating until complete dissolution. To a 20 mL Pyrex vial,  $CH_3COOH$  (0.25 mL), 0.4 M  $Zr(O^iPr)_4$  solution in  $CH_3COOH$  (0.05 mL, 0.02 mmol), DMF (4 – X mL), 0.02 M N-boc-BPDC solution (1 mL, 0.02 mmol) and DMF suspension of Bpy-UiO-

67(Zr) (X mL, 0.0191 mmol) were added sequentially. The mixture was vortexed for 10 seconds and stirred at 120 rpm in a 65 °C for 10, 20, 60, 120, 300, 1440 or 2880 minutes. Suspensions were then centrifuged at 10,000 rpm for 3 minutes obtain a white precipitate, Bpy-UiO-67(Zr) ⊂ N-boc-UiO-67(Zr). The precipitate was washed with fresh DMF (4 mL, 4x) and ACN (4 mL, 4x) and then soaked in an ACN solution of bis(acetonitrile)dichloropalladium(II) overnight. A subsequent ACN wash (6 x 6 mL) was conducted to remove excess uncoordinated palladium.

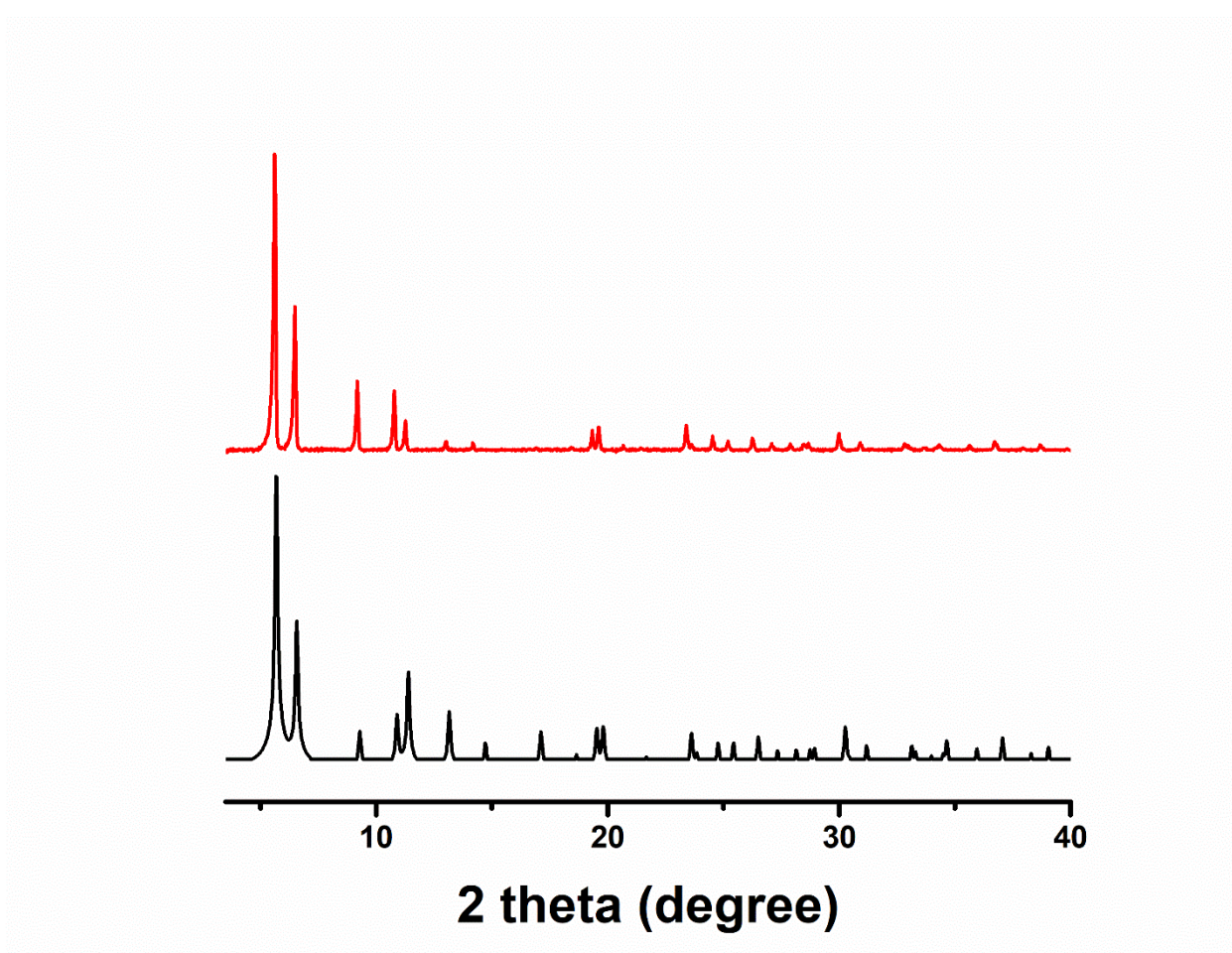
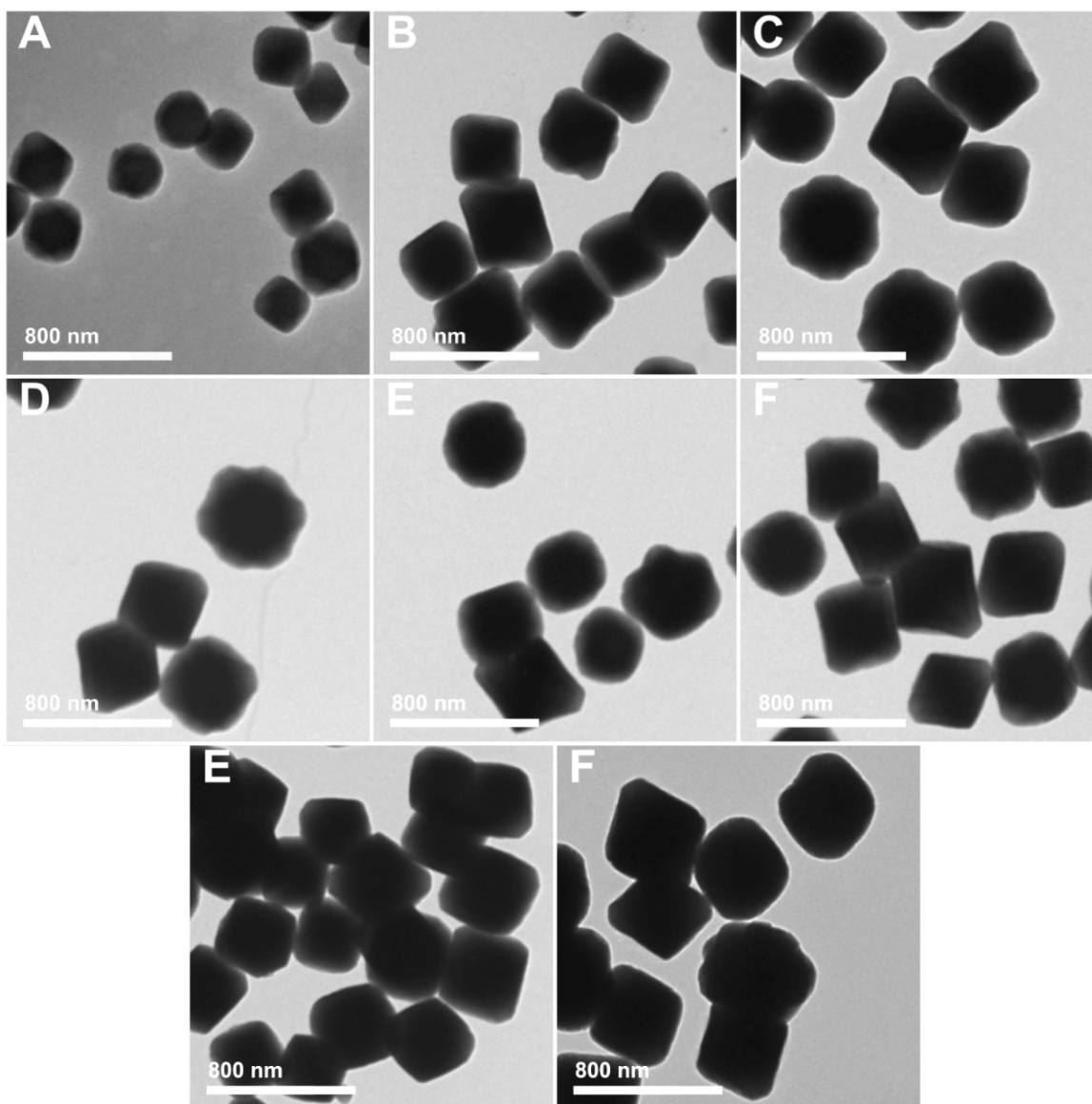


Figure 3.11 Simulated PXRD pattern of UiO-67(Zr) (black) and experimental PXRD of as synthesized Bpy-UiO-67(Zr) ⊂ N-boc-UiO-67(Zr) sMOF (red).



**Figure 3.12** TEM images of (A) Bpy-UiO-67(Zr) seed crystallites and Bpy-UiO-67(Zr)  $\subset$  N-boc-UiO-67(Zr) sMOFs after (B) 10 minutes, (C) 20 minutes, (D) 60 minutes, (E) 2 hours, (F) 5 hours, (G) 24 hours, (H) and 48 hours of reaction time.

**Table 3.3 Shell palladium to zirconium ratio calculated using STEM-EDS for Bpy(Pd)-UiO-67(Zr)  $\subset$  N-boc-UiO-67(Zr) synthesized with different reaction lengths.**

<b>Reaction Time (min)</b>	<b>Shell Pd/Zr</b>
10	$0.08 \pm 0.01$
20	$0.08 \pm 0.01$
60	$0.09 \pm 0.01$
120	$0.12 \pm 0.02$
300	$0.19 \pm 0.06$
1440	$0.30 \pm 0.02$
2440	$0.28 \pm 0.01$

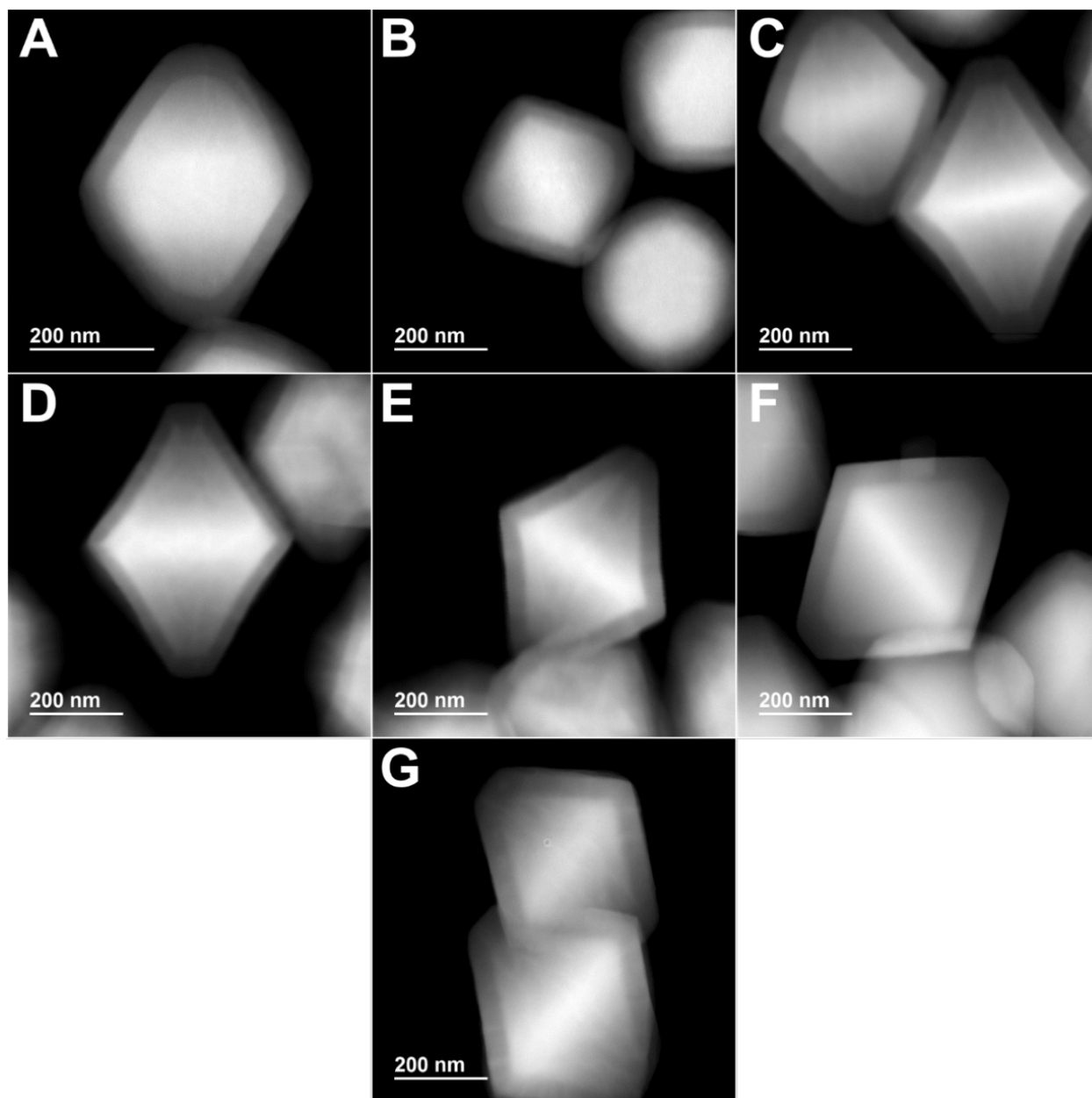


**Figure 3.13** HAADF TEM images of Bpy(Pd)-UiO-67(Zr)  $\subset$  N-boc-UiO-67(Zr) sMOFs after (A) 10 minutes, (B) 20 minutes, (C) 60 minutes, (D) 2 hours, (E) 5 hours, (F) 24 hours, and (G) 48 hours of reaction time.

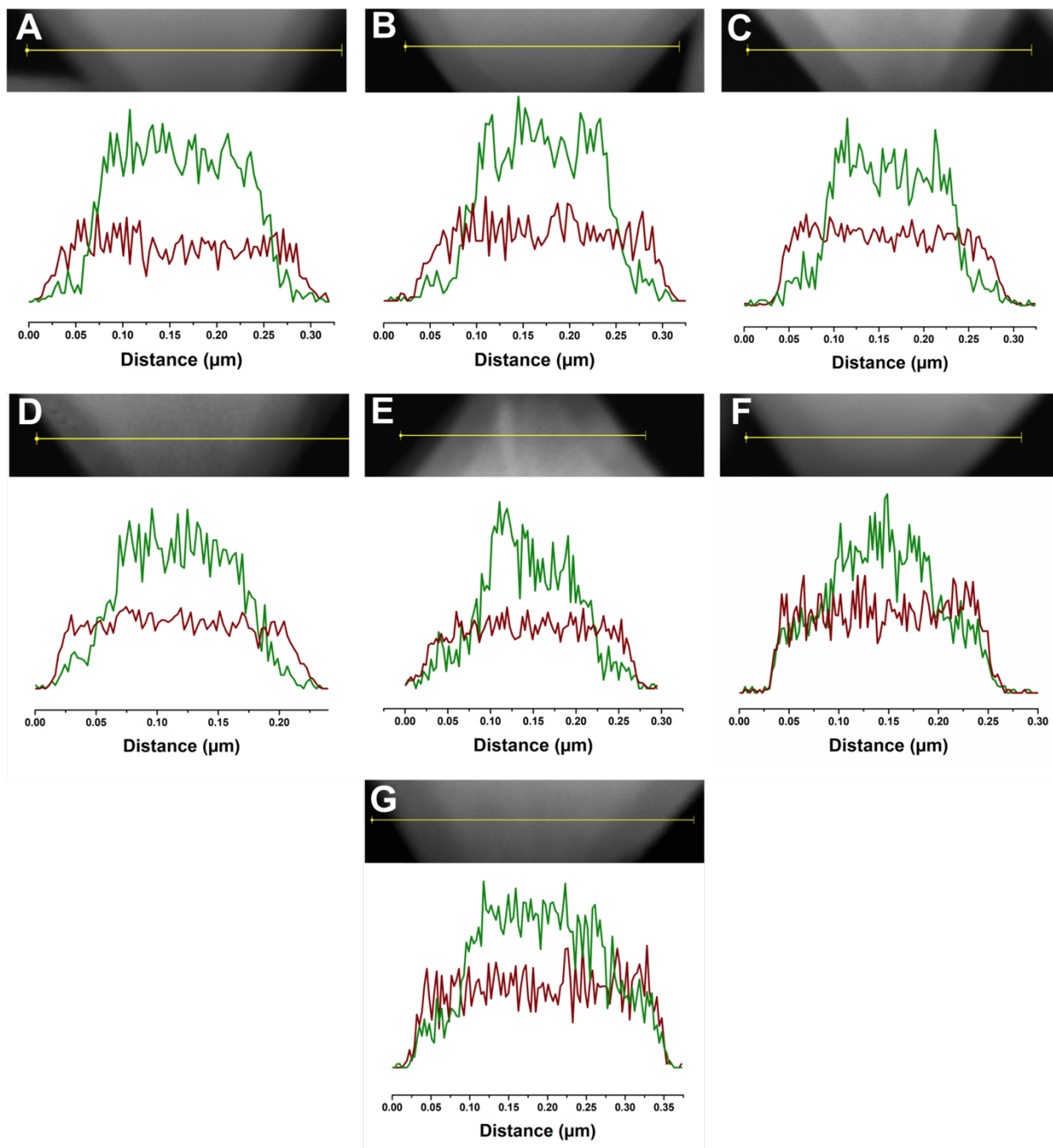


**Figure 3.14** STEM-EDS line-scans of Bpy(Pd)-UiO-67(Zr)  $\subset$  N-boc-UiO-67(Zr) sMOFs (Zr, red; Pd, green) after (A) 10 minutes, (B) 20 minutes, (C) 60 minutes, (D) 2 hours, (E) 5 hours, (F) 24 hours, and (G) 48 hours of reaction time.

### 3.3.6 Synthesis of Bpy-UiO-67(Zr) ⊂ Proline-boc-UiO-67(Zr) sMOF

0.4 M solution of  $Zr(O^iPr)_4$  in  $CH_3COOH$  was prepared by mixing  $Zr(O^iPr)_4$  70 wt. % in n-propanol (187.2 mg, 0.4 mmol) with  $CH_3COOH$  (1 mL). A 0.02 M solution of (S)-2-(1-(tert-butoxycarbonyl)pyrrolidine-2-carboxamido)-BPDC (proline-boc-BPDC) was prepared by adding proline-boc-BPDC (36 mg, 0.08 mmol) to DMF (4 mL) and sonicating until complete dissolution. To a 20 mL Pyrex vial,  $CH_3COOH$  (0.3 mL), 0.4 M  $Zr(O^iPr)_4$  solution in  $CH_3COOH$  (0.05 mL, 0.02 mmol), DMF (4 – X mL), 0.02 M  $H_2$ -Pro-BPDC solution (1 mL, 0.02 mmol) and DMF suspension of Bpy-UiO-67(Zr) (X mL, 0.0191 mmol) were added sequentially. The mixture was vortexed for 10 seconds and stirred at 120 rpm in a 65 °C oil bath for 10, 20, 60, 120, 300, 1440 or 2880 minutes. Suspensions were then centrifuged at 10,000 rpm for 3 minutes obtain a white precipitate, Bpy-UiO-67(Zr) ⊂ Proline-boc-UiO-67(Zr). The precipitate was washed with fresh DMF (4 mL, 4x) and ACN (4 mL, 4x) and then soaked in an ACN solution of bis(acetonitrile)dichloropalladium(II) overnight. A subsequent ACN wash (6 x 6 mL) was conducted to remove excess uncoordinated palladium.

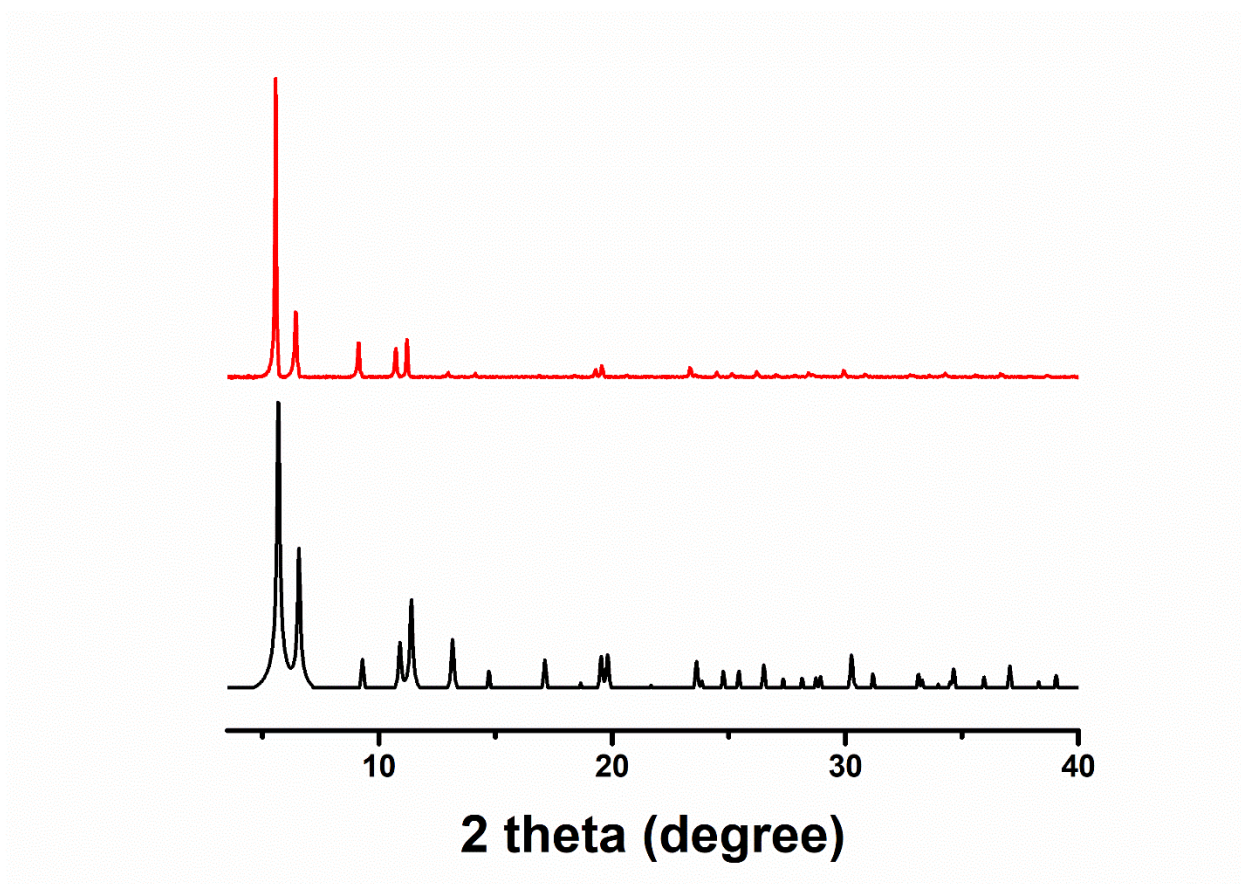
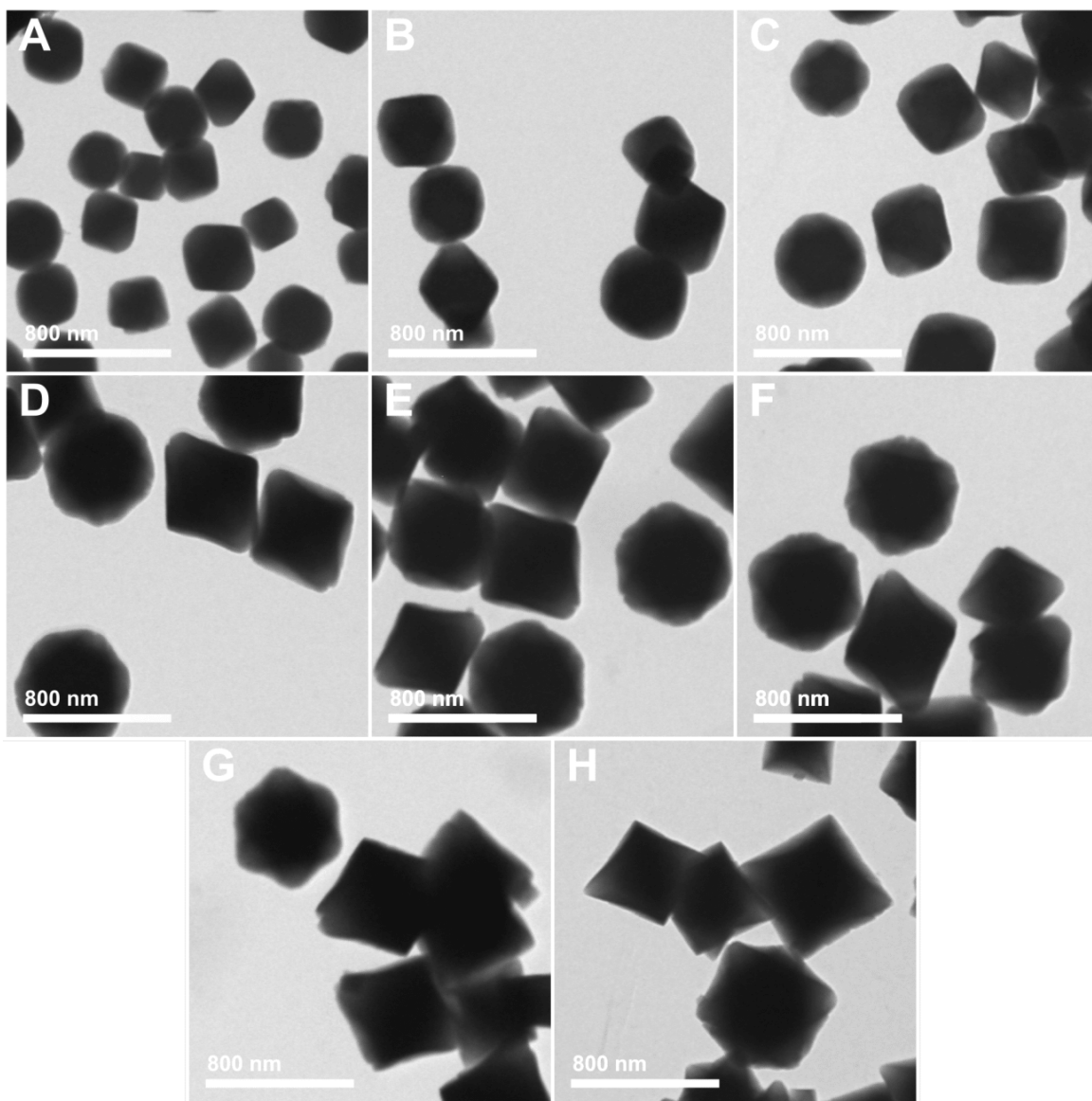


Figure 3.15 Simulated PXRD pattern of UiO-67(Zr) (black) and experimental PXRD of as synthesized Bpy-UiO-67(Zr) ⊂ Proline-boc-UiO-67(Zr) sMOF (red).



**Figure 3.16** TEM images of (A) Bpy-UiO-67(Zr) seed crystallites and Bpy-UiO-67(Zr)  $\subset$  Proline-boc-UiO-67(Zr) sMOFs after (B) 10 minutes, (C) 20 minutes, (D) 60 minutes, (E) 2 hours, (F) 5 hours, (G) 24 hours, (H) and 48 hours of reaction time.

**Table 3.4 Shell palladium to zirconium ratio calculated using STEM-EDS for Bpy(Pd)-UiO-67(Zr)  $\subset$  Proline-boc-UiO-67(Zr) synthesized with different reaction lengths. Shells observed after 10 minutes of reaction were not thick enough to get accurate reading.**

<b>Reaction Time (min)</b>	<b>Shell Pd/Zr</b>
20	$0.09 \pm 0.01$
60	$0.09 \pm 0.01$
240	$0.10 \pm 0.01$
300	$0.15 \pm 0.03$
1440	$0.18 \pm 0.06$
2440	$0.21 \pm 0.06$

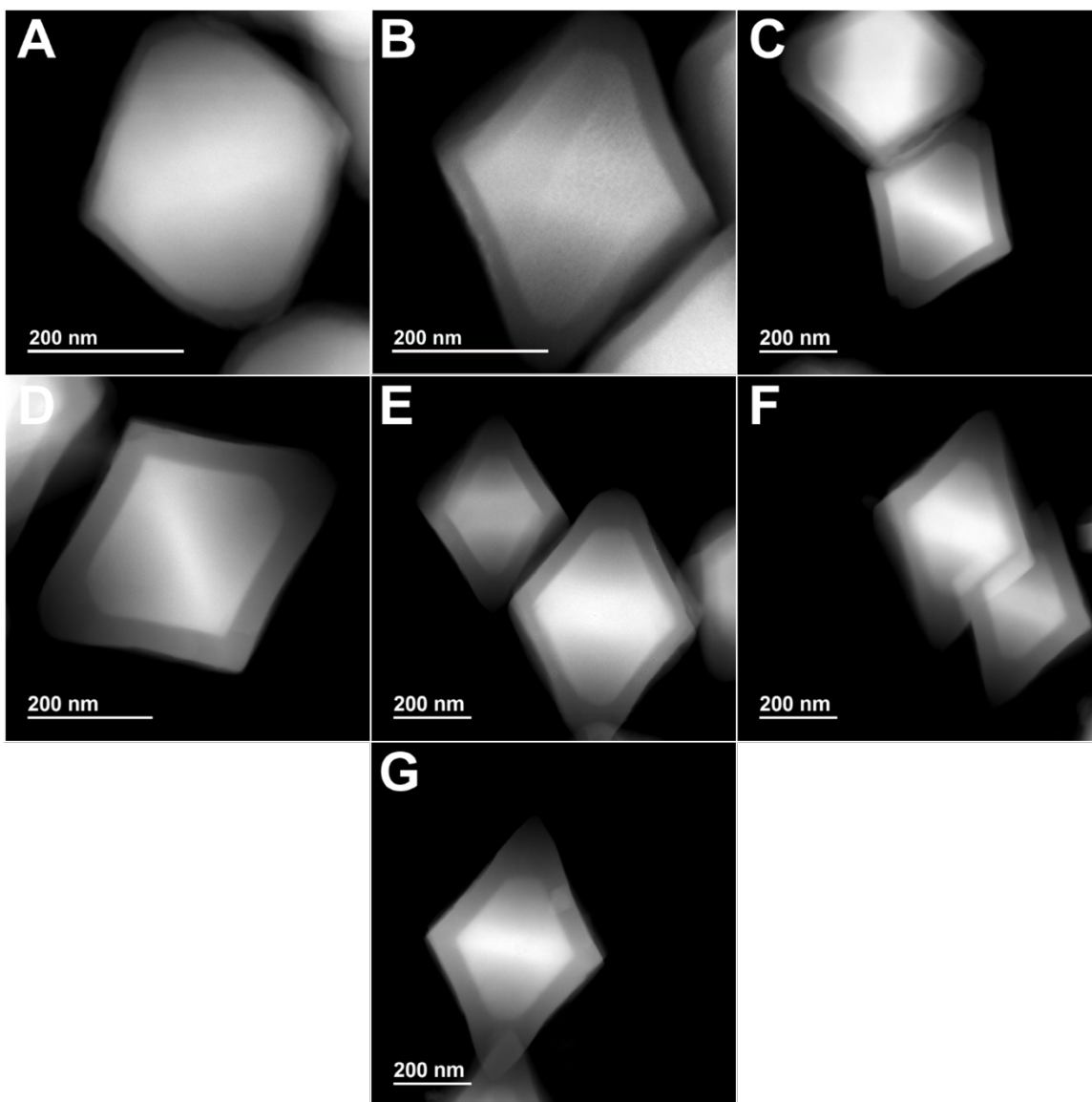


**Figure 3.17** HAADF TEM images of Bpy(Pd)-UiO-67(Zr)  $\subset$  Proline-boc-UiO-67(Zr) sMOFs after (A) 10 minutes, (B) 20 minutes, (C) 60 minutes, (D) 2 hours, (E) 5 hours, (F) 24 hours, and (G) 48 hours of reaction time.

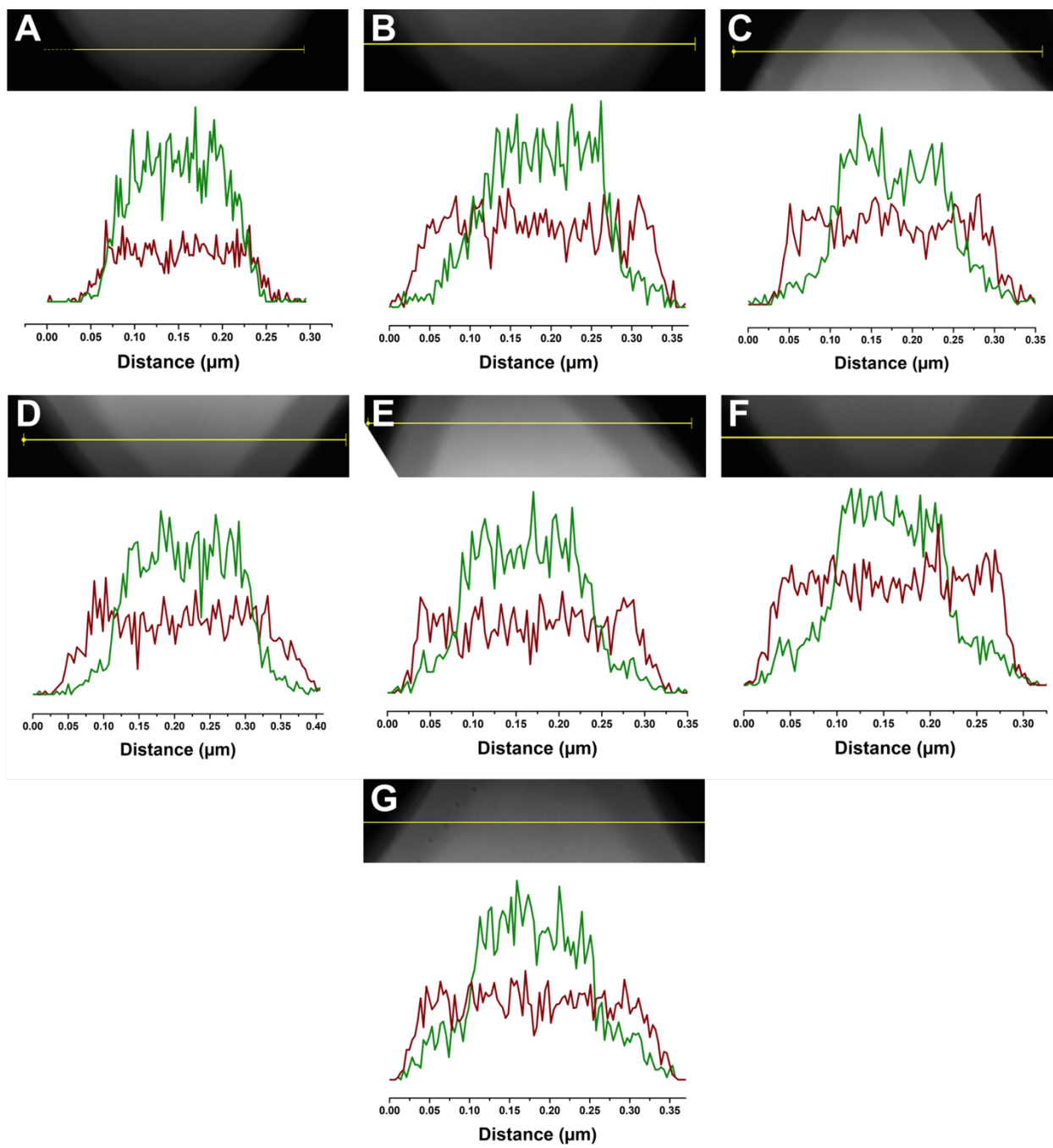


**Figure 3.18** STEM-EDS line-scans of Bpy(Pd)-UiO-67(Zr)  $\subset$  Proline-boc-UiO-67(Zr) sMOFs (Zr, red; Pd, green) after (A) 10 minutes, (B) 20 minutes, (C) 60 minutes, (D) 2 hours, (E) 5 hours, (F) 24 hours, and (G) 48 hours of reaction time.

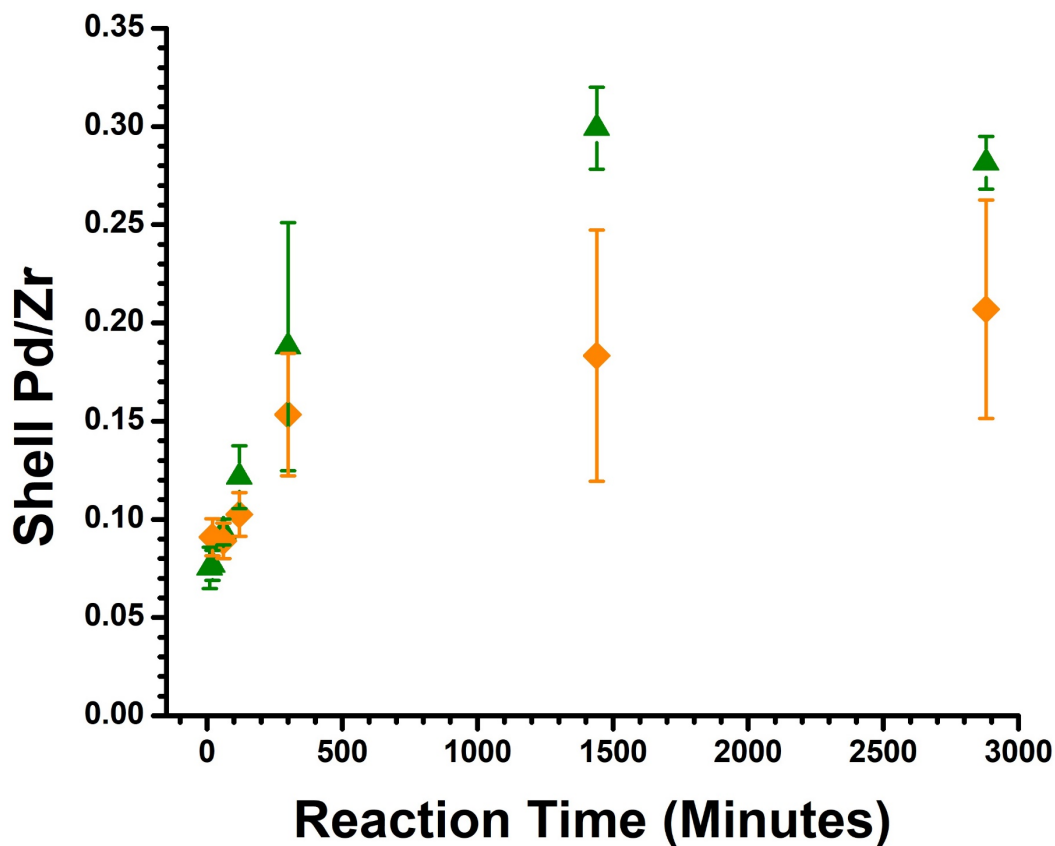


Figure 3.19 Shell palladium to zirconium ratios of Bpy(Pd)-UiO-67(Zr)  $\subset$  N-boc-UiO-67(Zr) (green) and Bpy(Pd)-UiO-67(Zr)  $\subset$  Proline-boc-UiO-67(Zr) (orange) sMOFs for reaction times of up to 48 hours long.

### 3.3.7 Synthesis of Bpy-UiO-67(Zr) $\subset$ Proline-boc-UiO-67(Zr) $\subset$ UiO-67(Zr) sMOF

0.4 M solution of  $Zr(O^iPr)_4$  in  $CH_3COOH$  was prepared by mixing  $Zr(O^iPr)_4$  70 wt. % in n-propanol (187.2 mg, 0.4 mmol) with  $CH_3COOH$  (1 mL). A 0.02 M solution of (S)-2-(1-(tert-butoxycarbonyl)pyrrolidine-2-carboxamido)-BPDC (proline-boc-BPDC) was prepared by adding proline-boc-BPDC (36 mg, 0.08 mmol) to DMF (4 mL) and sonicating until complete dissolution. To a 20 mL Pyrex vial,  $CH_3COOH$  (0.3 mL), 0.4 M  $Zr(O^iPr)_4$  solution in  $CH_3COOH$  (0.05 mL, 0.02 mmol), DMF (4 – X mL), 0.02 M  $H_2$ -Pro-BPDC solution (1 mL, 0.02 mmol) and DMF

suspension of Bpy-UiO-67(Zr) (X mL, 0.0191 mmol) were added sequentially. The mixture was vortexed for 10 seconds and stirred at 120 rpm in a 65 °C oil bath for 5 minutes. Suspensions were then centrifuged at 10,000 rpm for 3 minutes obtain a white precipitate, Bpy-UiO-67(Zr)  $\subset$  Proline-boc-UiO-67(Zr). The precipitate was washed with fresh DMF (4 mL, 4x) and suspended in 1 mL of DMF.

A 0.02 M solution of H<sub>2</sub>-BPDC was prepared by heating a mixture of H<sub>2</sub>-BPDC (19.4 mg, 0.08 mmol) and DMF (4 mL) on a stir plate at 150 °C until complete dissolution. To a 20 mL Pyrex vial, CH<sub>3</sub>COOH (0.3 mL), 0.4 M Zr(O<sup>n</sup>Pr)<sub>4</sub> solution in CH<sub>3</sub>COOH (0.05 mL, 0.02 mmol), DMF (3 mL), 0.02 M H<sub>2</sub>-BPDC solution (1 mL, 0.02 mmol) and DMF suspension of Bpy-UiO-67(Zr)  $\subset$  Proline-boc-UiO-67(Zr) (1 mL, 0.0191 mmol) were added sequentially. The mixture was vortexed for 10 seconds and stirred at 120 rpm in a 65 °C oil bath for 20 minutes. Suspensions were then centrifuged at 10,000 rpm for 3 minutes obtain a white precipitate, Bpy-UiO-67(Zr)  $\subset$  Proline-boc-UiO-67(Zr)  $\subset$  UiO-67(Zr). The precipitate was washed with fresh DMF (4 mL, 4x), ACN (4 mL, 4x) and then soaked in an ACN solution of bis(acetonitrile)dichloropalladium(II) overnight. A subsequent ACN wash (6 x 6 mL) was conducted to remove excess uncoordinated palladium.

### 3.4 Strata Stability in Solvent

The compositional integrity of strata in sMOFs were testing through soaking in dimethylformamide (DMF), water, Acetonitrile (ACN), chloroform and hexanes at 25 °C and elevated temperatures. In each case, synthesized sMOFs were washed with DMF (4 x 4 mL), followed by a wash with the soaking solvent (4 x 4 mL). After soaking, crystals were washed with

acetonitrile (4 x 4 mL) and soaked in an acetonitrile solution of bis(acetonitrile)dichloropalladium(II) overnight. A subsequent ACN wash (6 x 6 mL) was conducted to remove excess uncoordinated palladium.

### 3.4.1 Stability of Bpy-UiO-67(Zr) $\subset$ UiO-67(Zr) in DMF at 100 °C

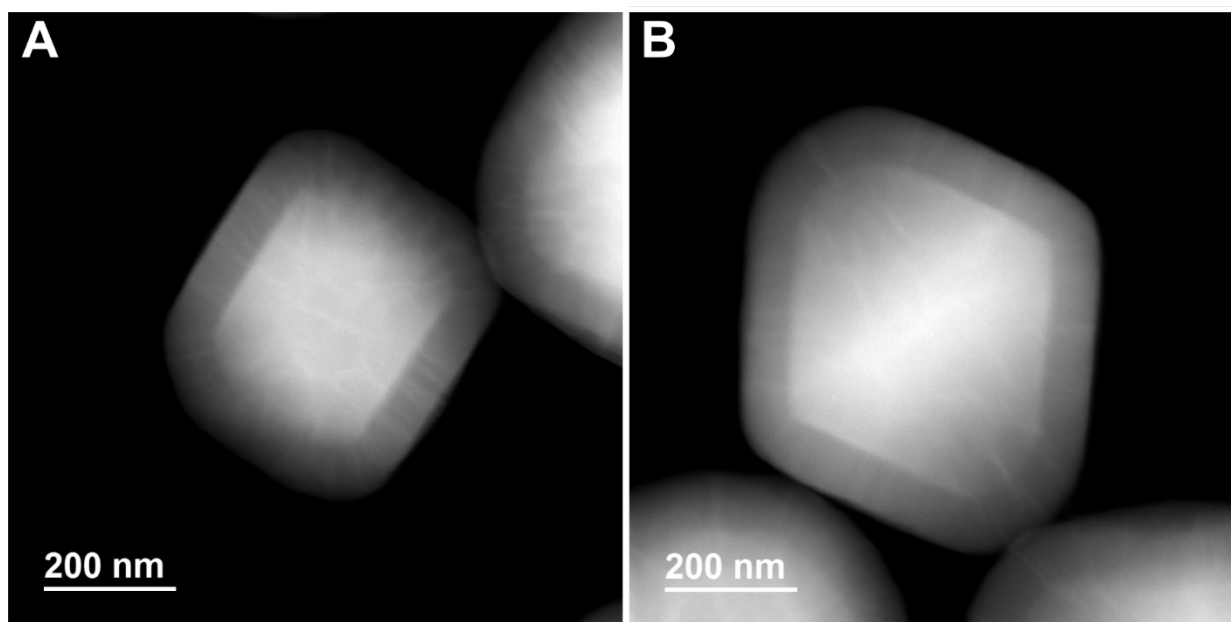


Figure 3.20 HAADF TEM images of Bpy(Pd)-UiO-67(Zr)  $\subset$  UiO-67(Zr) sMOFs (A) before soaking and (B) 48 hours of soaking in DMF at 100 °C.

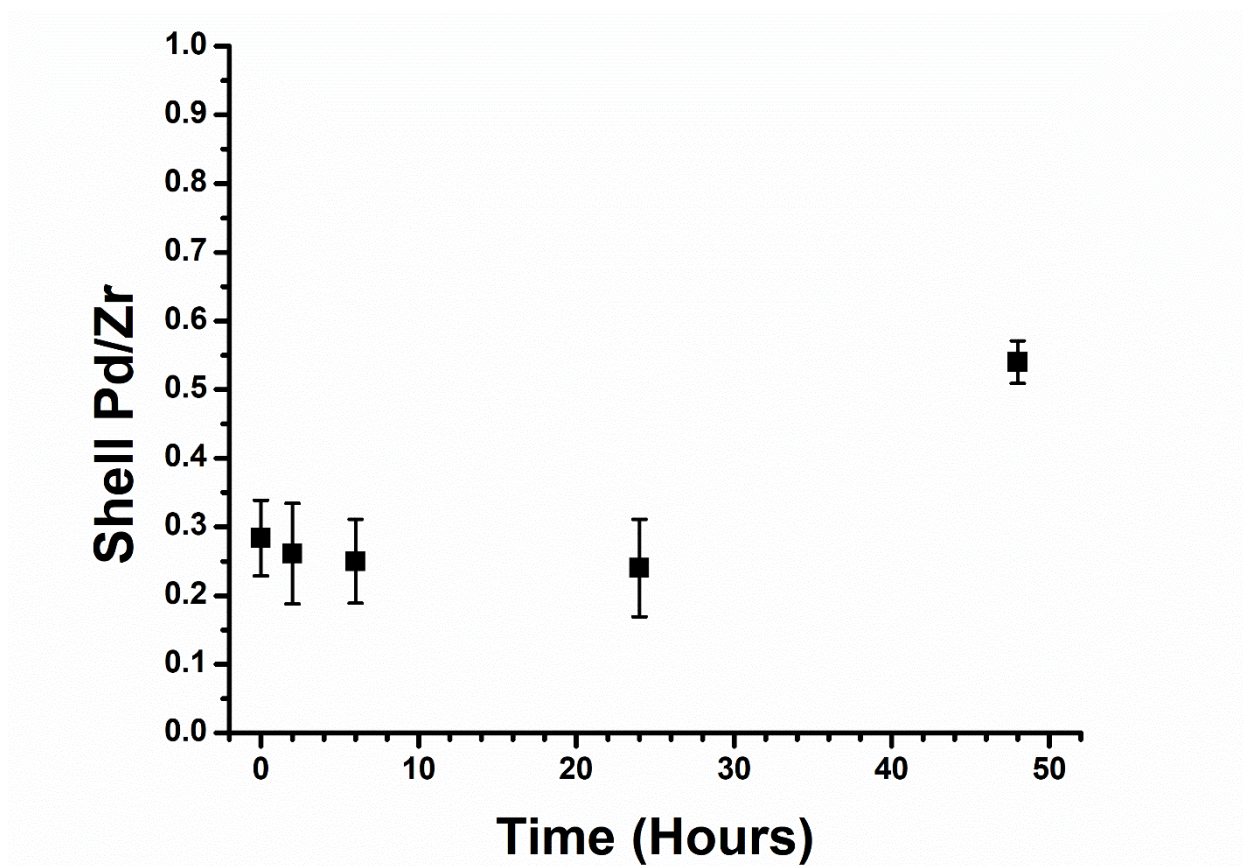


Figure 3.21 Shell palladium to zirconium ratio of Bpy(Pd)-UiO-67(Zr)  $\subset$  UiO-67(Zr) sMOFs soaked in DMF at 100 °C for up to 48 hours.

### 3.4.2 Stability of Bpy-UiO-67(Zr) $\subset$ UiO-67(Zr) in water at 85 °C

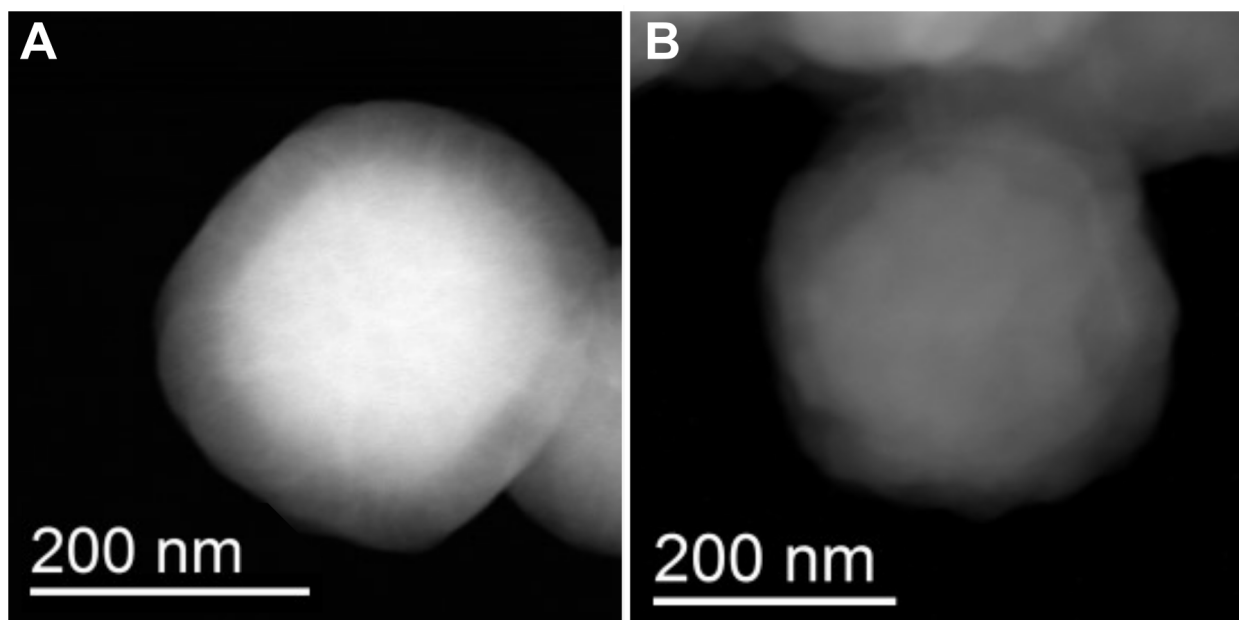


Figure 3.22 HAADF TEM images of Bpy(Pd)-UiO-67(Zr)  $\subset$  UiO-67(Zr) sMOFs (A) before soaking and (B) 21 hours of soaking in water at 85 °C.

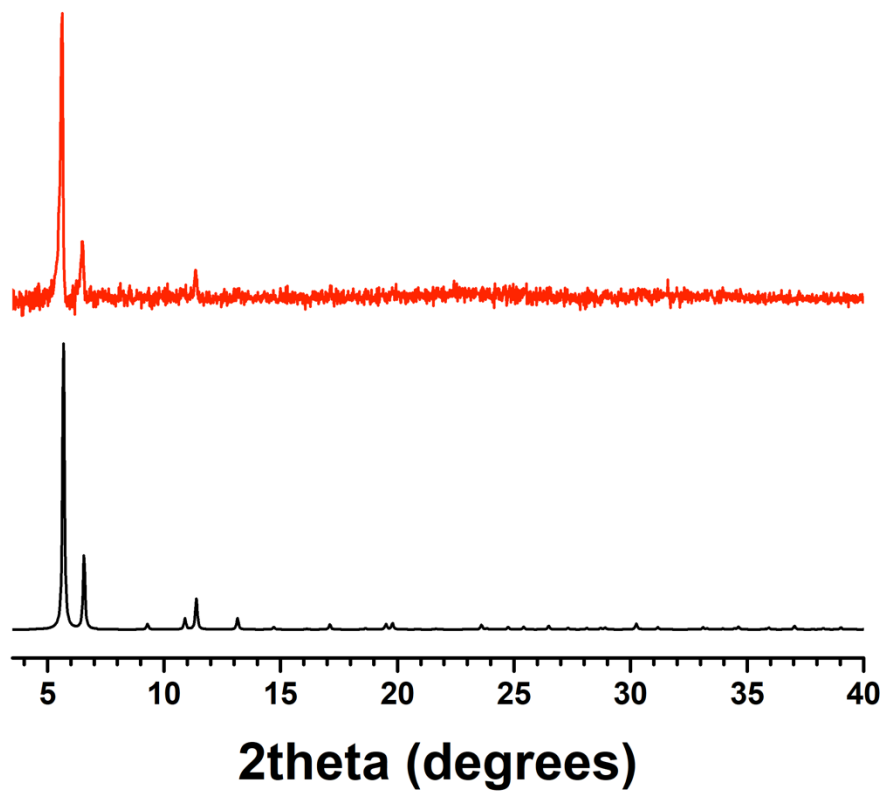


Figure 3.23 Simulated PXRD pattern of UiO-67(Zr) (black) and experimental PXRD of Bpy-UiO-67(Zr) sMOF after 21 hours of soaking in water at 85 °C (red).

### 3.4.3 Stability of Bpy-UiO-67(Zr) $\subset$ UiO-67(Zr) in DMF and CH<sub>3</sub>COOH at 65 °C

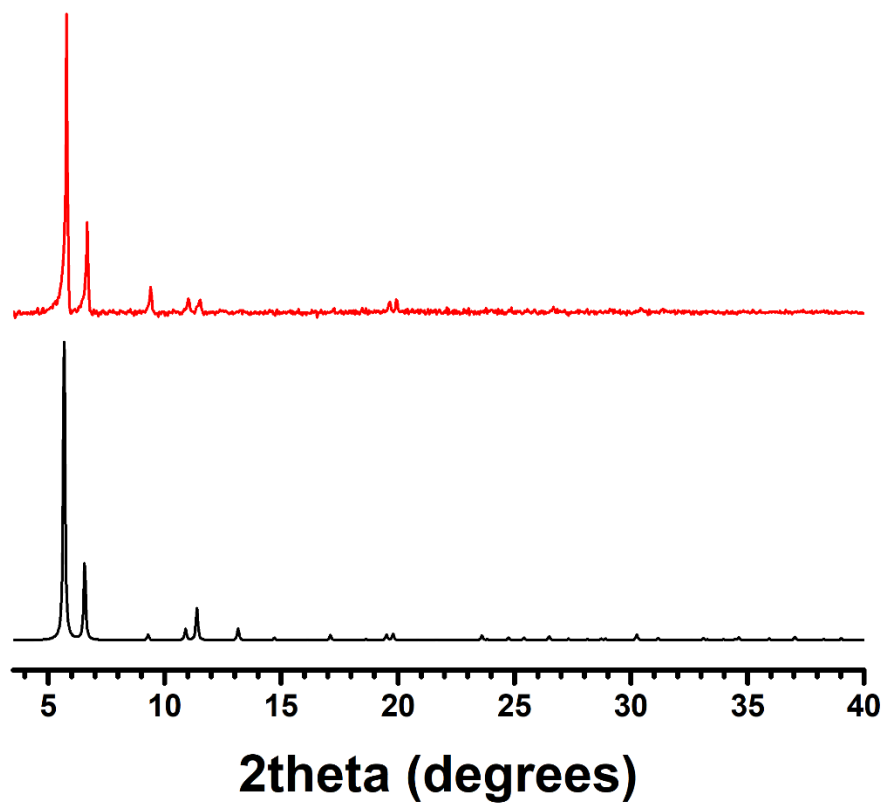


Figure 3.24 Simulated PXRD pattern of UiO-67(Zr) (black) and experimental PXRD of Bpy-UiO-67(Zr)  $\subset$  UiO-67(Zr) sMOF after 2 hours of soaking in DMF and CH<sub>3</sub>COOH at 65 °C (red).

# Appendix A Reproduction Permissions

**ACS Publications**  
Most Trusted Most Cited Most Read

**Coordination Assemblies from a Pd(II)-Cornered Square Complex**  
Author: Makoto Fujita, Masahide Tomimaga, Akiko Hori, et al  
Publication: Accounts of Chemical Research  
Publisher: American Chemical Society  
Date: Apr 1, 2005  
Copyright © 2005, American Chemical Society

**Quick Price Estimate**

This service provides permission for reuse only. If you do not have a copy of the portion you are using, you may copy and paste the content and reuse according to the terms of your agreement. Please be advised that obtaining the content you license is a separate transaction not involving RightsLink.

If credit is given to another source for the material you requested from RightsLink, permission must be obtained from that source.  
Note: Individual Scheme and Structure reuse is free of charge and does not require a license. If the scheme or structure is identified as a "Figure" in the article, permission is required.

Permission for this particular request is granted for print and electronic formats, and translations, at no charge. Figures and tables may be modified. Appropriate credit should be given. Please print this page for your records and provide a copy to your publisher. Requests for up to 4 figures require only this record. Five or more figures will generate a printout of additional terms and conditions. Appropriate credit should read: "Reprinted with permission from (COMPLETE REFERENCE CITATION). Copyright (YEAR) American Chemical Society." Insert appropriate information in place of the capitalized words.  
If credit is given to another source for the material you requested, permission must be obtained from that source.

I would like to...  Format

Requestor Type  Select your currency

Portion  Quick Price

Number of Table/Figure/Micrographs

[QUICK PRICE](#) [CONTINUE](#)

To request permission for a type of use not listed, please contact the publisher directly.

## Permission 1.

**Science**  
MAAAS

**Systematic Design of Pore Size and Functionality in Isoreticular MOFs and Their Application in Methane Storage**  
Author: Mohamed Eddoudi, Jaheon Kim, Nathaniel Rossi, David Vodak, Joseph Wachter, Michael O'Keefe, Omar M. Yaghi  
Publication: Science  
Publisher: The American Association for the Advancement of Science  
Date: Jan 18, 2002  
Copyright © 2002, The American Association for the Advancement of Science

**Order Completed**

Thank you for your order.  
This Agreement between Mathews De Souza ("You") and The American Association for the Advancement of Science ("The American Association for the Advancement of Science") consists of your license details and the terms and conditions provided by The American Association for the Advancement of Science and Copyright Clearance Center.

Your confirmation email will contain your order number for future reference.

License Number: 5062000058537 [Printable Details](#)

License date: May 04, 2021

Licensed Content		Order Details	
Licensed Content Publisher	The American Association for the Advancement of Science	Type of Use	Thesis / Dissertation
Licensed Content Publication	Science	Requestor type	Scientists/Individual at a research institution
Licensed Content Title	Systematic Design of Pore Size and Functionality in Isoreticular MOFs and Their Application in Methane Storage	Format	Electronic
Licensed Content Author	Mohamed Eddoudi, Jaheon Kim, Nathaniel Rossi, David Vodak, Joseph Wachter, Michael O'Keefe, Omar M. Yaghi	Portion	Text Excerpt
Licensed Content Date	Jan 18, 2002	Number of pages requested	1
Licensed Content Volume	295		
Licensed Content Issue	5554		

About Your Work		Additional Data	
Title	Leveraging Ligand Steric Demand to Control Linker Exchange and Fine-Tune Domain Building Block Composition in Stratified Metal-Organic Frameworks	Portions	Scheme 1, and Figure 1
Institution name	University of Pittsburgh		
Expected presentation date	May 2021		

## Permission 2.

## Bibliography

- (1) Zhou, S.-F.; Zhong, W.-Z. Drug Design and Discovery: Principles and Applications. *Molecules* **2017**, *22* (2), 279. <https://doi.org/10.3390/molecules22020279>.
- (2) Ariga, K.; Nishikawa, M.; Mori, T.; Takeya, J.; Shrestha, L. K.; Hill, J. P. Self-Assembly as a Key Player for Materials Nanoarchitectonics. *Sci. Technol. Adv. Mater.* **2019**, *20* (1), 51–95. <https://doi.org/10.1080/14686996.2018.1553108>.
- (3) Boles, M. A.; Engel, M.; Talapin, D. V. Self-Assembly of Colloidal Nanocrystals: From Intricate Structures to Functional Materials. *Chem. Rev.* **2016**, *116* (18), 11220–11289. <https://doi.org/10.1021/acs.chemrev.6b00196>.
- (4) Whitesides, G. M.; Boncheva, M. Beyond Molecules: Self-Assembly of Mesoscopic and Macroscopic Components. *Proc. Natl. Acad. Sci.* **2002**, *99* (8), 4769–4774. <https://doi.org/10.1073/pnas.082065899>.
- (5) Sender, R.; Fuchs, S.; Milo, R. Revised Estimates for the Number of Human and Bacteria Cells in the Body. *PLOS Biol.* **2016**, *14* (8), e1002533. <https://doi.org/10.1371/journal.pbio.1002533>.
- (6) Biedermann, F.; Schneider, H.-J. Experimental Binding Energies in Supramolecular Complexes. *Chem. Rev.* **2016**, *116* (9), 5216–5300. <https://doi.org/10.1021/acs.chemrev.5b00583>.
- (7) Lehn, J.-M. Perspectives in Supramolecular Chemistry—From Molecular Recognition towards Molecular Information Processing and Self-Organization. *Angew. Chem. Int. Ed. Engl.* **1990**, *29* (11), 1304–1319. <https://doi.org/10.1002/anie.199013041>.
- (8) Schneider, H.-J. Binding Mechanisms in Supramolecular Complexes. *Angew. Chem. Int. Ed.* **2009**, *48* (22), 3924–3977. <https://doi.org/10.1002/anie.200802947>.
- (9) Whitesides, G. M. Self-Assembly at All Scales. *Science* **2002**, *295* (5564), 2418–2421. <https://doi.org/10.1126/science.1070821>.

- (10) Diercks, C. S.; Yaghi, O. M. The Atom, the Molecule, and the Covalent Organic Framework. *Science* **2017**, *355* (6328), eaal1585. <https://doi.org/10.1126/science.aal1585>.
- (11) Lehn, J.-M. Toward Complex Matter: Supramolecular Chemistry and Self-Organization. *Proc. Natl. Acad. Sci.* **2002**, *99* (8), 4763–4768. <https://doi.org/10.1073/pnas.072065599>.
- (12) Lehn, J.-M. Supramolecular Chemistry—Scope and Perspectives Molecules, Supermolecules, and Molecular Devices(Nobel Lecture). *Angew. Chem. Int. Ed. Engl.* **1988**, *27* (1), 89–112. <https://doi.org/10.1002/anie.198800891>.
- (13) Pedersen, C. J. The Discovery of Crown Ethers (Noble Lecture). *Angew. Chem. Int. Ed. Engl.* **1988**, *27* (8), 1021–1027. <https://doi.org/10.1002/anie.198810211>.
- (14) Cram, D. J. The Design of Molecular Hosts, Guests, and Their Complexes (Nobel Lecture). *Angew. Chem. Int. Ed. Engl.* **1988**, *27* (8), 1009–1020. <https://doi.org/10.1002/anie.198810093>.
- (15) Lehn, J. M.; Sawage, J. P. SYNTHESSES ET PROPRIETES PHYSIQUES DE SYSTEMES DIAZA-POLYOXA-MACROBICYCLIQUES". 17.
- (16) Pedersen, C. J. Cyclic Polyethers and Their Complexes with Metal Salts. *J. Am. Chem. Soc.* **1967**, *20*.
- (17) Lehn, J.-M. Supramolecular Chemistry and Chemical Synthesis. In *Chemical Synthesis*; Chatgililoglu, C., Snieckus, V., Eds.; Springer Netherlands: Dordrecht, 1996; pp 511–524. [https://doi.org/10.1007/978-94-009-0255-8\\_22](https://doi.org/10.1007/978-94-009-0255-8_22).
- (18) Dinolfo, P. H.; Hupp, J. T. Supramolecular Coordination Chemistry and Functional Microporous Molecular Materials. 13.
- (19) Fujita, M.; Yazaki, J.; Ogura, K. Preparation of a Macrocyclic Polynuclear Complex, [(En)Pd(4,4'-Bpy)]<sub>4</sub>(NO<sub>3</sub>)<sub>8</sub> (En = Ethylenediamine, Bpy = Bipyridine), Which Recognizes an Organic Molecule in Aqueous Media. *J. Am. Chem. Soc.* **1990**, *112* (14), 5645–5647. <https://doi.org/10.1021/ja00170a042>.

- (20) Fujita, M.; Tominaga, M.; Hori, A.; Therrien, B. Coordination Assemblies from a Pd(II)-Cornered Square Complex. *Acc. Chem. Res.* **2005**, *38* (4), 369–378. <https://doi.org/10.1021/ar040153h>.
- (21) Fujita, M.; Oguro, D.; Miyazawa, M.; Oka, H.; Yamaguchit, K.; Ogura, K. Self-Assembly of Ten Molecules into Nanometre-Sized Organic Host Frameworks. **1995**, *378*, 3.
- (22) Beissel, T.; Powers, R. E.; Raymond, K. N. Symmetry-Based Metal Complex Cluster Formation. *Angew. Chem. Int. Ed. Engl.* **1996**, *35* (10), 1084–1086. <https://doi.org/10.1002/anie.199610841>.
- (23) Kusakawa, T.; Fujita, M. “Ship-in-a-Bottle” Formation of Stable Hydrophobic Dimers of *Cis*-Azobenzene and -Stilbene Derivatives in a Self-Assembled Coordination Nanocage. *J. Am. Chem. Soc.* **1999**, *121* (6), 1397–1398. <https://doi.org/10.1021/ja9837295>.
- (24) Kumazawa, K.; Yamanoi, Y.; Yoshizawa, M.; Kusakawa, T.; Fujita, M. A Palladium(II)-Clipped Aromatic Sandwich. *Angew. Chem. Int. Ed.* **2004**, *43* (44), 5936–5940. <https://doi.org/10.1002/anie.200460868>.
- (25) Yaghi, O. M.; Li, G.; Li, H. Selective Binding and Removal of Guests in a Microporous Metal–Organic Framework. *Nature* **1995**, *378* (6558), 703–706. <https://doi.org/10.1038/378703a0>.
- (26) Yaghi, O. M.; Li, H. Hydrothermal Synthesis of a Metal–Organic Framework Containing Large Rectangular Channels. *J. Am. Chem. Soc.* **1995**, *117* (41), 10401–10402. <https://doi.org/10.1021/ja00146a033>.
- (27) Li, H.; Eddaoudi, M.; O’Keeffe, M.; Yaghi, O. M. Design and Synthesis of an Exceptionally Stable and Highly Porous Metal–Organic Framework. *Nature* **1999**, *402* (6759), 276–279. <https://doi.org/10.1038/46248>.
- (28) Eddaoudi, M. Systematic Design of Pore Size and Functionality in Isoreticular MOFs and Their Application in Methane Storage. *Science* **2002**, *295* (5554), 469–472. <https://doi.org/10.1126/science.1067208>.
- (29) Rosi, N. L. Hydrogen Storage in Microporous Metal–Organic Frameworks. *Science* **2003**, *300* (5622), 1127–1129. <https://doi.org/10.1126/science.1083440>.

- (30) Rowsell, J. L. C.; Yaghi, O. M. Metal–Organic Frameworks: A New Class of Porous Materials. *Microporous Mesoporous Mater.* **2004**, *73* (1–2), 3–14. <https://doi.org/10.1016/j.micromeso.2004.03.034>.
- (31) Farha, O. K.; Eryazici, I.; Jeong, N. C.; Hauser, B. G.; Wilmer, C. E.; Sarjeant, A. A.; Snurr, R. Q.; Nguyen, S. T.; Yazaydin, A. Ö.; Hupp, J. T. Metal–Organic Framework Materials with Ultrahigh Surface Areas: Is the Sky the Limit? *J. Am. Chem. Soc.* **2012**, *134* (36), 15016–15021. <https://doi.org/10.1021/ja3055639>.
- (32) Kayal, S.; Sun, B.; Chakraborty, A. Study of Metal-Organic Framework MIL-101(Cr) for Natural Gas (Methane) Storage and Compare with Other MOFs (Metal-Organic Frameworks). *Energy* **2015**, *91*, 772–781. <https://doi.org/10.1016/j.energy.2015.08.096>.
- (33) Yang, W.; Chang, G.; Wang, H.; Hu, T.-L.; Yao, Z.; Alfooty, K.; Xiang, S.; Chen, B. A Three-Dimensional Tetraphenylethene-Based Metal-Organic Framework for Selective Gas Separation and Luminescence Sensing of Metal Ions: A Three-Dimensional Tetraphenylethene-Based Metal-Organic Framework for Selective Gas Separation and Luminescence Sensing of Metal Ions. *Eur. J. Inorg. Chem.* **2016**, *2016* (27), 4470–4475. <https://doi.org/10.1002/ejic.201600201>.
- (34) Fischer, M.; Gomes, J. R. B.; Fröba, M.; Jorge, M. Modeling Adsorption in Metal–Organic Frameworks with Open Metal Sites: Propane/Propylene Separations. *Langmuir* **2012**, *28* (22), 8537–8549. <https://doi.org/10.1021/la301215y>.
- (35) Ding, L.; Yazaydin, A. O. Hydrogen and Methane Storage in Ultrahigh Surface Area Metal–Organic Frameworks. *Microporous Mesoporous Mater.* **2013**, *6*.
- (36) Dhakshinamoorthy, A.; Li, Z.; Garcia, H. Catalysis and Photocatalysis by Metal Organic Frameworks. *Chem. Soc. Rev.* **2018**, *47* (22), 8134–8172. <https://doi.org/10.1039/C8CS00256H>.
- (37) Lee, J.; Farha, O. K.; Roberts, J.; Scheidt, K. A.; Nguyen, S. T.; Hupp, J. T. Metal–Organic Framework Materials as Catalysts. *Chem. Soc. Rev.* **2009**, *38* (5), 1450. <https://doi.org/10.1039/b807080f>.

- (38) An, J.; Farha, O. K.; Hupp, J. T.; Pohl, E.; Yeh, J. I.; Rosi, N. L. Metal-Adeninate Vertices for the Construction of an Exceptionally Porous Metal-Organic Framework. *Nat. Commun.* **2012**, *3*, 604.
- (39) Luo, T.-Y.; Das, P.; White, D. L.; Liu, C.; Star, A.; Rosi, N. L. Luminescence “Turn-On” Detection of Gossypol Using Ln<sup>3+</sup>-Based Metal–Organic Frameworks and Ln<sup>3+</sup> Salts. *J. Am. Chem. Soc.* **2020**, *142* (6), 2897–2904. <https://doi.org/10.1021/jacs.9b11429>.
- (40) Furukawa, H.; Cordova, K. E.; O’Keeffe, M.; Yaghi, O. M. The Chemistry and Applications of Metal-Organic Frameworks. *Science* **2013**, *341* (6149), 1230444–1230444. <https://doi.org/10.1126/science.1230444>.
- (41) Deng, H.; Doonan, C. J.; Furukawa, H.; Ferreira, R. B.; Towne, J.; Knobler, C. B.; Wang, B.; Yaghi, O. M. Multiple Functional Groups of Varying Ratios in Metal-Organic Frameworks. *Science* **2010**, *327* (5967), 846–850. <https://doi.org/10.1126/science.1181761>.
- (42) Ockwig, N. W.; Delgado-Friedrichs, O.; O’Keeffe, M.; Yaghi, O. M. Reticular Chemistry: Occurrence and Taxonomy of Nets and Grammar for the Design of Frameworks. *Acc. Chem. Res.* **2005**, *38* (3), 176–182. <https://doi.org/10.1021/ar020022l>.
- (43) Tranchemontagne, D. J.; Ni, Z. Reticular Chemistry of Metal-Organic Polyhedra. *MO* **2008**, *12*.
- (44) Yaghi, O. M. Reticular Chemistry—Construction, Properties, and Precision Reactions of Frameworks. *J. Am. Chem. Soc.* **2016**, *138* (48), 15507–15509. <https://doi.org/10.1021/jacs.6b11821>.
- (45) Zhou, H.-C.; Long, J. R.; Yaghi, O. M. Introduction to Metal–Organic Frameworks. *Chem. Rev.* **2012**, *112* (2), 673–674. <https://doi.org/10.1021/cr300014x>.
- (46) Yuan, S.; Feng, L.; Wang, K.; Pang, J.; Bosch, M.; Lollar, C.; Sun, Y.; Qin, J.; Yang, X.; Zhang, P.; Wang, Q.; Zou, L.; Zhang, Y.; Zhang, L.; Fang, Y.; Li, J.; Zhou, H.-C. Stable Metal-Organic Frameworks: Design, Synthesis, and Applications. *Adv. Mater.* **2018**, *30* (37), 1704303. <https://doi.org/10.1002/adma.201704303>.
- (47) Helal, A.; Yamani, Z. H.; Cordova, K. E.; Yaghi, O. M. Multivariate Metal-Organic Frameworks. *Natl. Sci. Rev.* **2017**, *4* (3), 296–298. <https://doi.org/10.1093/nsr/nwx013>.

- (48) Luo, T.-Y.; Liu, C.; Gan, X. Y.; Muldoon, P. F.; Diemler, N. A.; Millstone, J. E.; Rosi, N. L. Multivariate Stratified Metal–Organic Frameworks: Diversification Using Domain Building Blocks. *J. Am. Chem. Soc.* **2019**, *141* (5), 2161–2168. <https://doi.org/10.1021/jacs.8b13502>.
- (49) Liu, C.; Rosi, N. L. Ternary Gradient Metal–Organic Frameworks. *Faraday Discuss.* **2017**, *201*, 163–174. <https://doi.org/10.1039/C7FD00045F>.
- (50) Liu, C.; Zeng, C.; Luo, T.-Y.; Merg, A. D.; Jin, R.; Rosi, N. L. Establishing Porosity Gradients within Metal–Organic Frameworks Using Partial Postsynthetic Ligand Exchange. *J. Am. Chem. Soc.* **2016**, *138* (37), 12045–12048. <https://doi.org/10.1021/jacs.6b07445>.
- (51) Kim, M.; Cahill, J. F.; Fei, H.; Prather, K. A.; Cohen, S. M. Postsynthetic Ligand and Cation Exchange in Robust Metal–Organic Frameworks. *J. Am. Chem. Soc.* **2012**, *134* (43), 18082–18088. <https://doi.org/10.1021/ja3079219>.
- (52) Lerma-Berlanga, B.; R. Ganivet, C.; Almora-Barrios, N.; Tatay, S.; Peng, Y.; Albero, J.; Fabelo, O.; González-Platas, J.; García, H.; M. Padial, N.; Martí-Gastaldo, C. Effect of Linker Distribution in the Photocatalytic Activity of Multivariate Mesoporous Crystals. *J. Am. Chem. Soc.* **2021**, *143* (4), 1798–1806. <https://doi.org/10.1021/jacs.0c09015>.
- (53) Boissonnault, J. A.; Wong-Foy, A. G.; Matzger, A. J. Core–Shell Structures Arise Naturally During Ligand Exchange in Metal–Organic Frameworks. *J. Am. Chem. Soc.* **2017**, *139* (42), 14841–14844. <https://doi.org/10.1021/jacs.7b08349>.
- (54) Cavka, J. H.; Jakobsen, S.; Olsbye, U.; Guillou, N.; Lamberti, C.; Bordiga, S.; Lillerud, K. P. A New Zirconium Inorganic Building Brick Forming Metal Organic Frameworks with Exceptional Stability. *J. Am. Chem. Soc.* **2008**, *130* (42), 13850–13851. <https://doi.org/10.1021/ja8057953>.
- (55) Liu, C.; Li, T.; Rosi, N. L. Strain-Promoted “Click” Modification of a Mesoporous Metal–Organic Framework. *J. Am. Chem. Soc.* **2012**, *134* (46), 18886–18888. <https://doi.org/10.1021/ja307713q>.
- (56) Deshpande, R. K.; Minnaar, J. L.; Telfer, S. G. Thermolabile Groups in Metal–Organic Frameworks: Suppression of Network Interpenetration, Post-Synthetic Cavity Expansion,

and Protection of Reactive Functional Groups. *Angew. Chem. Int. Ed.* **2010**, *49* (27), 4598–4602. <https://doi.org/10.1002/anie.200905960>.

- (57) Lun, D. J.; Waterhouse, G. I. N.; Telfer, S. G. A General Thermolabile Protecting Group Strategy for Organocatalytic Metal–Organic Frameworks. *J. Am. Chem. Soc.* **2011**, *133* (15), 5806–5809. <https://doi.org/10.1021/ja202223d>.
- (58) Rama, G.; Ardá, A.; Maréchal, J.-D.; Gamba, I.; Ishida, H.; Jiménez-Barbero, J.; Vázquez, M. E.; Vázquez López, M. Stereoselective Formation of Chiral Metallopeptides. *Chem. - Eur. J.* **2012**, *18* (23), 7030–7035. <https://doi.org/10.1002/chem.201201036>.